Systems/Circuits

Regulation of the Mouse Ventral Tegmental Area by Melanin-Concentrating Hormone

Carl Duncan Spencer, Persephone A. Miller, Jesukhogie G. Williams-Ikhenoba, Ralitsa G. Nikolova, and Melissa J. Chee

Department of Neuroscience, Carleton University, Ottawa, Ontario K1S 5B6, Canada

Melanin-concentrating hormone (MCH) acts via its sole receptor MCHR1 in rodents and is an important regulator of homeostatic behaviors like feeding, sleep, and mood to impact overall energy balance. The loss of MCH signaling by MCH or MCHR1 deletion produces hyperactive mice with increased energy expenditure, and these effects are consistently associated with a hyperdopaminergic state. We recently showed that MCH suppresses dopamine release in the nucleus accumbens, which principally receives dopaminergic projections from the ventral tegmental area (VTA), but the mechanisms underlying MCH-regulated dopamine release are not clearly defined. MCHR1 expression is widespread and includes dopaminergic VTA cells. However, as the VTA is a neurochemically diverse structure, we assessed *Mchr1* gene expression at glutamatergic, GABAergic, and dopaminergic VTA cells and determined if MCH inhibited the activity of VTA cells and/or their local microcircuit. *Mchr1* expression was robust in major VTA cell types, including most dopaminergic (78%) or glutamatergic cells (52%) and some GABAergic cells (38%). Interestingly, MCH directly inhibited dopaminergic and GABAergic cells but did not regulate the activity of glutamatergic cells. Rather, MCH produced a delayed increase in excitatory input to dopamine cells and a corresponding decrease in GABAergic input to glutamatergic VTA cells. Our findings suggested that MCH may acutely suppress dopamine release while disinhibiting local glutamatergic signaling to restore dopamine levels. This indicated that the VTA is a target of MCH action, which may provide bidirectional regulation of energy balance.

Key words: disinhibition; dopamine; electrophysiology; hypothalamus; MCHR1; mesolimbic

> ## Significance Statement
>
> The role of melanin-concentrating hormone (MCH) on energy balance may converge on the dopamine system via the mesolimbic pathway, as the loss of MCH or MCH receptor (MCHR1) signaling increases hyperactivity and energy expenditure associated with a hyperdopaminergic state. MCH can suppress dopamine release within the mesolimbic pathway, but its underlying mechanism is not known. We thus determined if MCH could inhibit dopamine release through direct actions within the ventral tegmental area (VTA). We found that MCH directly inhibited dopaminergic VTA cells, but MCH also disinhibited excitatory input to dopamine cells. Therefore, we showed that the VTA is a putative target site supporting dopamine-dependent actions of MCH.

Introduction

Melanin-concentrating hormone (MCH) is produced largely in the lateral hypothalamic zone to promote positive energy balance by acting through its receptor MCHR1. MCHR1 is a G-protein–coupled receptor (Chambers et al., 1999; Lembo et al., 1999; Saito

et al., 1999) and typically inhibits cells via $G_{i/o}$ activation (Gao and van den Pol, 2001). Mice overexpressing *Mch* may overeat and develop diet-induced obesity (Ludwig et al., 2001), while *Mch* knock-out (*Mch-KO*) mice are lean and hyperactive and have an increased metabolic rate (Shimada et al., 1998; Kokkotou et al., 2005). Similarly, *Mchr1* deletion also results in leanness, hyperactivity, and increased energy expenditure (Chen et al., 2002; Marsh et al., 2002; Åstrand et al., 2004). Although MCH administration stimulates feeding (Qu et al., 1996; Sears et al., 2010), transgenic models of *Mch* or *Mchr1* deletion do not similarly effect feeding (Lord et al., 2022). In contrast, hyperactivity and increased energy expenditure are consistent features following the transgenic *Mch* or *Mchr1* deletion.

A hyperdopaminergic state underlies the hyperactivity of *Mch-* or *Mchr1-KO* animals. There is an elevated amount of dopamine in the accumbens nucleus of *Mch-KO* mice (Pissios

et al., 2008) and rats (Mul et al., 2011). Furthermore, treating *Mch-KO* mice with a dopamine reuptake inhibitor leads to greater accumulation of dopamine at the accumbens, and this can enhance hyperlocomotor activity (Pissios et al., 2008). Consistently, MCH can suppress dopamine release in the accumbens, and the inhibitory actions of MCH are mediated in part by *Mchr1* expression at GABAergic accumbens neurons (Chee et al., 2019).

Dopaminergic afferents in the accumbens originate from the ventral tegmental area (VTA; Albanese and Minciacchi, 1983) and form the mesolimbic pathway that is implicated in the regulation of reward and motivation. The VTA is a heterogeneous area comprising dopaminergic, GABAergic, and glutamatergic cells (Morales and Margolis, 2017), as well as cells that are both GABAergic and glutamatergic (Yamaguchi et al., 2007; Root et al., 2014a), dopaminergic and GABAergic (Tritsch et al., 2012; Stamatakis et al., 2013), or dopaminergic and glutamatergic (Sulzer et al., 1998; Dal Bo et al., 2004; Stuber et al., 2010; Tecuapetla et al., 2010). Interestingly, dopaminergic VTA neurons receive inputs from local GABA and glutamate cells (Morales and Margolis, 2017), but other brain regions, such as the lateral hypothalamic area, projecting to the VTA may also regulate dopaminergic VTA neurons (Nieh et al., 2016).

MCH neurons may directly innervate multiple VTA cell types, including GABAergic, glutamatergic, and dopaminergic cells (Faget et al., 2016). Optogenetic activation of MCH neurons can increase dopamine release in the accumbens and increase sucrose preference over a nonnutritive sweetener (Domingos et al., 2013). However, *Mch-KO* mice do not show deficits in nutrient-sensing because the nutritive value associated with sucrose is ascribed to glutamate release from MCH neurons (Schneeberger et al., 2018). Nevertheless, this does not preclude direct MCH actions on VTA neurons that can inhibit dopamine release.

The VTA comprises MCH-immunoreactive fibers (Bittencourt et al., 1992) and *Mchr1* mRNA (Hervieu et al., 2000), but the identity of MCHR1-expressing VTA cells and mechanism(s) of MCH action in the VTA have not been defined. We determined *Mchr1* mRNA expression on GABAergic, glutamatergic, or dopaminergic VTA cells identified by the vesicular GABA transporter (*Vgat*), vesicular glutamate transporter 2 (*Vglut2*), or tyrosine hydroxylase (TH), respectively. We found that MCH directly hyperpolarized dopaminergic or GABAergic VTA cells but not glutamatergic cells. As VTA dopamine cells receive both GABAergic and glutamatergic afferents (Morales and Margolis, 2017), we also determined if MCH may regulate GABAergic or glutamatergic synaptic transmission at dopaminergic VTA cells. Interestingly, MCH did not alter GABAergic transmission at dopaminergic VTA cells, but it produced a delayed increase in the glutamatergic input. This may reflect a disinhibition of the glutamatergic tone onto dopamine cells in the VTA, as MCH can suppress GABAergic transmission at glutamate cells. These findings supported both direct and indirect MCH action that regulates neuronal activity or synaptic transmission at dopaminergic VTA cells.

Materials and Methods

All animal procedures were approved by the Animal Care Committee at Carleton University. All mice were bred on a C57BL/6J background and group housed in a 12:12 h light/dark cycle with *ad libitum* access to water and standard mouse chow (Teklad Global Diets 2014, Envigo).

Quantitative real-time PCR

Wild-type (WT) mice 6–20 weeks old ($N = 16$) were anesthetized with an intraperitoneal (i.p.) injection of 7% chloral hydrate (700 mg/kg). The

brain was rapidly removed from the skull, and samples of the striatum, hypothalamus, hippocampus, cerebellum, and VTA were microdissected and flash-frozen in liquid nitrogen. Tissue samples were homogenized in TRIzol (Invitrogen), and RNA was isolated by chloroform and precipitated by isopropanol. The RNA pellet was washed with 70% ethanol and air-dried before resuspending in distilled water. RNA purity was determined by a 260/280 absorbance ratio of ~2.0 using a NanoDrop Lite Spectrophotometer (Thermo Fisher Scientific).

RNA samples were treated with DNase and reverse transcribed for cDNA synthesis with an iScript gDNA Clear cDNA Synthesis Kit (1725035, Bio-Rad Laboratories). We performed quantitative RT-PCR using a CFX Connect Real-Time PCR Detection System thermal cycler (1855201, Bio-Rad Laboratories). Custom primers (Invitrogen) for mouse glyceraldehyde-3-phosphate dehydrogenase (*Gapdh*) and *Mchr1* mRNA comprised the following sequences: *Gapdh* forward, 5′-ATGTGTCCGTCGTGGATCTGA-3′; *Gapdh* reverse, 5′-ATGCC TGCTTCACCACCTTCTT-3′; *Mchr1* forward, 5′-CAATGCCAG CAACATCTCC-3′; and *Mchr1* reverse, 5′-ACCAAACACTGAAGG CATGA-3′.

Mchr1 mRNA expression in each brain region was calculated via double-delta cycle threshold analysis and standardized to the expression levels of *Gapdh* of the same mouse. Relative *Mchr1* mRNA expression in each brain region was then normalized to the level of *Mchr1* mRNA in the hypothalamus for each sex.

Histology

Tissue preparation. Mice (12–20 weeks old) were anesthetized with 7% chloral hydrate (700 mg/kg, i.p.) and underwent transcardiac perfusion with cold (4°C) sterile saline (0.9% NaCl) followed by prechilled (4°C) phosphate-buffered formalin (10%; VWR).

Immunohistochemistry (IHC). Brain tissues from WT ($N = 6$) and *Mchr1-KO* mice ($N = 2$) were postfixed in 20% sucrose prepared in formalin (4 h) and then cryoprotected with 20% sucrose prepared in phosphate-buffered saline (PBS), pH 7.4, for 16 h until sectioning using a freezing microtome (Spencer Lens) into five series of 30 μm coronal sections. MCHR1 immunoreactivity was labeled as previously described (Diniz et al., 2020). In brief, the brain tissue was treated with 0.3% hydrogen peroxide and incubated with a rabbit anti-MCHR1 antibody (1:1,000; PA5-24182, UC2738292, Invitrogen) for 48 h at 4°C in a 3% normal donkey serum (NDS) solution. The tissue was thoroughly rinsed, incubated with a biotinylated donkey anti-rabbit IgG antibody (1:500; 711-065-152, Lot 101909, Jackson ImmunoResearch Laboratories) at room temperature (RT) for 1 h, and treated with avidin–biotin–horseradish peroxidase (1:1:833; PK-6100, Vector Laboratories) at RT for 30 min before incubating with 0.5% biotinylated (EZ-Link Sulfo-NHS-LC-Biotin; Thermo Fisher Scientific) tyramine (Sigma-Aldrich; Sigma Chemical) for 20 min (RT). All sections were then incubated with an Alexa Fluor 647-conjugated streptavidin (1:500; 016-600-084, Lot 135095, Jackson ImmunoResearch Laboratories) and NeuroTrace (1:50; N21479, Thermo Fisher Scientific) for 2 h at RT. Following staining, all tissues were thoroughly rinsed and immediately mounted onto Superfrost Plus microscope glass slides (Thermo Fisher Scientific) and coverslipped with ProLong Diamond Antifade mounting media (P36961, Invitrogen).

After IHC processing for MCHR1 immunoreactivity, one additional series were incubated with a sheep anti-TH antibody (1:1,000; GTX82570, Lot 822005648, GeneTex) at RT overnight. Sections were then incubated with a donkey anti-sheep secondary antibody conjugated with Alexa Fluor 594 (1:500; 715-496-150, Lot 82079, Jackson ImmunoResearch Laboratories) and NeuroTrace (1:50) for 2 h at RT. Tissues were rinsed, immediately mounted, and coverslipped as described above.

Thick tissue IHC. Brain slices following patch-clamp recordings were fixed in formalin for at least 24 h, treated with a 2% Triton X-100 PBS solution for 45 min at RT to permeabilize the tissue, and then incubated with a sheep anti-TH primary antibody (1:1,000; GeneTex) at 4°C for 72 h. After rinsing, the tissue was incubated with a streptavidin-conjugated Cy3 (1:500; 016-160-084, Lot 146014, Jackson

ImmunoResearch Laboratories) and donkey anti-sheep conjugated with Cy5 (1:500; 713-176-147, Lot 70443, Jackson ImmunoResearch Laboratories) secondary antibodies. The tissues were then rinsed and immediately mounted onto Superfrost Plus microscope glass slides and coverslipped with ProLong Diamond Antifade mounting media.

Combined in situ hybridization (ISH) and IHC. Brains from WT mice (*N* = 6) were postfixed in 10% formalin overnight, cryoprotected in 20% sucrose with 0.5% sodium azide (24 h), and sectioned using a freezing microtome into five series of 30 μm coronal sections. The series designated for ISH were immediately mounted onto Superfrost Plus microscope slides, air-dried at RT (21–23°C; 1 h) and −20°C (30 min), and then stored at −80°C. Adjacent brain series were reserved for Nissl staining, RNAscope probe labeling, and negative control, respectively. One slide from a separate series served as the positive control. We determined the coexpression of *Mchr1* with *Slc32a1* (*Vgat*) and *Slc17a6* (*Vglut2*) by RNAscope-enabled ISH and with TH by subsequent IHC in the same brain tissue. ISH procedures were completed based on manufacturer instructions for RNAscope ISH on a fixed-frozen mouse brain tissue [Multiplex Fluorescent Reagent Kit v2 User Manual; Advanced Cell Diagnostics (ACD)] as previously described (Bono et al., 2022), unless indicated otherwise.

In brief, slide-mounted brain tissues were dehydrated in an ethanol gradient, treated with hydrogen peroxide and target retrieval procedure for 5 min (99°C), and then dehydrated and air-dried overnight (RT). Tissues of interest were isolated by drawing a hydrophobic barrier and treated with Protease III in a HybEZ oven (40°C, 30 min). Slides were then incubated with a cocktail of *Mm-Mchr1* (317491, ACD) in Channel 1 (C1), *Mm-Slc32a1-C2* in C2 (319191-C2, ACD), and *Mm-Slc17a6* in C3 (319171-C3, ACD) probes (40°C, 2 h). Concentrated *Mm-Slc32a1* C2 and *Mm-Slc17a6* C3 probes were added to the diluted *Mm-Mchr1* C1 probe at a ratio of 1:50. A volume of 5–8 drops of the probe mixture was added to each slide. *Bacillus* dihydrodipicolinate reductase (*dapB*, 320871, ACD) and *Mm-Ppib* (313911, ACD) probes were used as the negative and positive control, respectively. Hybridization signals were amplified by sequential incubation at 40°C with AMP-1 (30 min; 323101, ACD), AMP-2 (30 min; 323102, ACD), and AMP-3 (15 min; 323103, ACD).

C1 *Mchr1* hybridization was developed (40°C, 15 min with HRP-C1; 323104, ACD) and tyramide signal amplification (TSA) plus Opal 690 (1:750, 40°C, 30 min; FP1497001KT, Akoya Biosciences) and then quenched with HRP Blocker (40°C, 15 min; 323107, ACD). C2 *Vgat* and C3 *Vglut2* hybridization were sequentially developed with HRP-C2 (323105, ACD) with TSA plus Cyanine 3 (1:1,500; NEL44E001KT, PerkinElmer) and HRP-C3 (323106, ACD) with TSA plus Opal 520 (1:750; FP1487001KT, Akoya Biosciences). C2 signal was similarly quenched with HRP Blocker (40°C, 15 min) before proceeding to C3 development.

Following ISH of the probe tissue, the tissues were treated for IHC labeling of TH immunoreactivity based on ACD directions for combined ISH and IHC (Advanced Cell Diagnostics, 2020) and as previously described (Mickelsen et al., 2019). Tissues were blocked with 3% NDS solution prepared in PBS (700 μl) for 30 min (RT) and then incubated with anti-sheep TH primary antibody (1:1,000; GTX82570, Lot 822005648, GeneTex) for 2 h (RT). Slides were thoroughly rinsed in PBS and then incubated with a donkey anti-sheep secondary antibody conjugated with Alexa Fluor 594 (1:500; 715-496-150, Lot 82079, Jackson ImmunoResearch Laboratories) for 30 min (RT). Slides were rinsed in Wash Buffer (320058, ACD), treated with DAPI Reagent (323108, ACD) for 30 s (RT), and immediately coverslipped with ProLong Gold Antifade Mountant (Thermo Fisher Scientific). Slides were kept in a dark drying drawer at RT overnight and then transferred to −20°C for storage until imaging.

Nissl stain. Sections underwent Nissl staining as previously described (Negishi et al., 2020; Bono et al., 2022).

Microscopy
Bright-field imaging. The Nissl-stained tissue was acquired with a Nikon Eclipse Ti2 inverted microscope (Nikon Instruments) equipped with a motorized stage and DS-Ri2 color camera (Nikon) using a 10× Plan Apochromat objective (0.45 NA). Bright-field images were stitched at 20% overlap with the NIS-Elements software.

Confocal imaging. Images from the Nissl-stained tissue were aligned to tiled, overview confocal images showing the VTA in relation to other midbrain regions acquired using the 405 nm wavelength laser with a 4× Plan Apochromat objective (0.2 NA). Stitched, high-resolution confocal frames from IHC- and/or ISH-treated tissues were captured from within the overview image.

Confocal imaging of MCHR1 immunoreactivity underwent scans with a 10× and/or 20× (0.75 NA) Plan Apochromat objectives using a Nikon C2 confocal system. Images were acquired with a 405 and 647 nm wavelength laser to visualize NeuroTrace- and Alexa Fluor 647-labeled signals. The tissue that was also stained for TH had additional images acquired with a 561 nm wavelength laser to visualize Alexa Fluor 594-labeled signal, and fluorescence signals from the 561 and 647 nm channels were pseudocolored magenta and green, respectively.

Confocal imaging of combined ISH- and IHC-treated tissue underwent scans with 20× Plan Apochromat objective using a Nikon C2 confocal system and acquired with a 405, 488, and 647 nm wavelength laser to visualize DAPI-, Opal 520-, and Alexa Fluor 647-labeled signals for nuclear stains, *Vglut2* hybridization, and *Mchr1* hybridization, respectively. Simultaneously at the same optical section, Cyanine 3- and Alexa Fluor 594-labeled signals to visualize *Vgat* hybridization and TH were acquired by spectral imaging using a 561 nm wavelength excitation laser in the continuous band (CB) setting to generate a lambda stack acquired with sequential 10-nm bandwidths spanning the wavelength range of 580–640 nm. The spectral profiles were unmixed to separate Cyanine 3 and Alexa Fluor 594 signals, which were most distinguished at 590 and 620 nm, respectively, and then merged with signals acquired by the 405, 488, and 647 nm wavelength laser to generate one image file displaying signals from all five fluorophores.

Tissues that served as the negative control were also acquired using the same combination of conventional confocal and spectral unmixing for the probe tissue. Background fluorescence related to nonspecific binding from ISH treatment was determined using the negative control tissue by adjusting the lookup table (LUT) values for each of the three image channels to yield a resultant black image. The LUT range was then applied to images acquired from the probe tissue to subtract background fluorescence; thus, any remaining signal observed from the probe tissue was considered to be positive hybridization signals.

Confocal imaging of IHC-treated cells in the thick tissue underwent scans with a 20× Plan Apochromat objective in a Nikon C2 confocal system and acquired with a 488, 561, and 647 nm wavelength laser to visualize native EGFP fluorescence, Cy3-labeled signal for biocytin-filled cell, and Cy5-labeled signals for TH immunoreactivity, respectively. Cy3 signal was pseudocolored blue.

Neuroanatomical analyses
Plane-of-section analysis. Nissl or fluorescent-Nissl images were parcellated in Adobe Illustrator CS6 (Adobe) based on the regions defined by the *Allen Reference Atlas* (ARA; Dong, 2008), as previously described (Negishi et al., 2020; Bono et al., 2022). Parcellations for MCHR1-immunoreactive (MCHR1-ir) cells were directly applied from fluorescent-Nissl signals captured within the same image acquisition. High-magnification confocal images of ISH-treated tissues were indirectly parcellated from bright-field images of an adjacent Nissl-stained section, which was aligned to the low-magnification, overview confocal image of the probe tissue.

Identifying MCHR1- and TH-ir signals. Our MCHR1 antibody (1:1,000; PA5-24182, Invitrogen) labeled MCHR1 immunoreactivity at the primary cilium of neurons (Diniz et al., 2020). Only cilia, identified by their long spindle-like appearance >1 μm (Diniz et al., 2020; Bansal et al., 2021), associated with a NeuroTrace-labeled somata was counted as a MCHR1-expressing cell. Only TH staining at the somata that colocalized with DAPI-, NeuroTrace-, or EGFP-labeled cell was considered. Only signals within the boundaries of the VTA, as determined by our plane-of-section analysis, were included in our analyses.

Identifying hybridization signals. Signal criteria were independently established based on the signal-to-background level for each hybridization signal. *Mchr1* hybridization signal appeared as punctate "dots" with clusters centered tightly around a DAPI-labeled nucleus (Bono et al., 2022). *Vgat* hybridization appeared as dot clusters that took the shape of cell bodies and were colocalized to a DAPI-labeled nucleus. Compared with *Vgat* hybridization, dot clusters following *Vglut2* hybridization were less dense within the cell and may appear as punctate dots.

Mapping. A circle was placed over each positively labeled immunoreactive or hybridized cell, and the relative positions of the circles were transferred, as previously described (Negishi et al., 2020; Bono et al., 2022), to coronal brain atlas templates (Dong, 2008) to generate standardized maps of *Mchr1*, *Vglut2*, *Vgat*, and TH expression. Cell counts at each atlas level were determined from cells mapped and counted unilaterally.

A number of cells reported for IHC and combined ISH and IHC studies were corrected for oversampling, as previously described (Chee et al., 2013; Negishi et al., 2020; Bono et al., 2022), using the Abercrombie formula $P = A\left(\frac{M}{L+M}\right)$ (Abercrombie, 1946), where P is the corrected count, A is the original count, M is the mean tissue thickness (IHC, 13.6 µm; ISH + IHC, 10.9 µm) determined from five brain slices, and L is the mean cell diameter (IHC, 15.6 µm; ISH + IHC, 16.0 µm) determined from 80 cells.

Electrophysiology

Animals. *Th-cre;L10-Egfp*, *Vgat-cre;L10-Egfp*, and *Vglut2-cre; L10-Egfp* reporter mice were generated by crossing *Th-cre* (Lindeberg et al., 2004), *Vgat-cre* (028862, JAX; Vong et al., 2011), or *Vglut2-cre* (028863, JAX; Vong et al., 2011) mice, respectively, to homozygous *lox-STOP-lox-L10-Egfp* reporter mice (Krashes et al., 2014). All transgenic lines were kindly provided by Dr. B. B. Lowell (Beth Israel Deaconess Medical Center).

Acute slice preparation. Mice (4–10 weeks old) were anesthetized with 7% chloral hydrate (700 mg/kg, i.p.) and transcardially perfused with ice-cold, carbogenated (95% O_2, 5% CO_2) slice artificial cerebrospinal fluid (ACSF) solution (300 mOsm/L),pH 7.4, containing the following (in mM): 92 NMDG, 2.5 KCl, 1.25 NaH_2PO_4, 30 $NaHCO_3$, 20 HEPES, 25 glucose, 2 thiourea, 5 Na-ascorbate, 3 Na-pyruvate, 0.5 $CaCl_2 \cdot 2H_2O$, and 10 $MgSO_4$ (Ting et al., 2018). Brains were sectioned on a vibratome (VT 1000S, Leica Biosystems) in slice ACSF to produce 250-µm-thick coronal slices that were immediately transferred to carbogenated slice solution at 37°C for 5 min. Slices were then incubated in a carbogenated bath ACSF (300 mOsm/L) containing the following (in mM), 124 NaCl, 3 KCl, 1.3 $MgSO_4$, 1.4 NaH_2PO_4, 10 D-glucose, 26 $NaHCO_3$, and 2.5 $CaCl_2$ for 5 min, and then allowed to recover in bath ACSF (RT) for at least 1 h prior to recordings.

Patch-clamp recordings. Brain slices containing the VTA, which primarily encompassed L83–87, were placed in a slice chamber, superfused (2–2.5 ml/min) with carbogenated bath ACSF prewarmed (37°C) by a temperature controller (Warner Instrument), and held in place by a platinum ring strung with nylon fiber made in-house.

VTA cells were visualized with infrared differential interference contrast microscopy at 40× magnification either on an Examiner.A1 microscope (Carl Zeiss) equipped with an AxioCam camera (Carl Zeiss) and AxioVision software (Carl Zeiss) or with an Eclipse FN1 microscope (Nikon) equipped with a pco.panda 4.2 camera (Excelitas PCO) and NIS-Elements Imaging software (Nikon). EGFP-labeled cells were identified using epifluorescence illumination from a halogen (HXP120, Carl Zeiss) or mercury lamp (C-SHG1, Nikon).

Borosilicate glass pipettes (593800; A-M Systems) were pulled on a P-1000 Flaming/Brown Micropipette Puller (Sutter Instrument) and backfilled (7–10 MΩ) with a potassium-based internal solution (290 mOsm/L), pH 7.24, containing the following (in mM): 120 K-gluconate, 10 KCl, 10 HEPES, 1 $MgCl_2$, 1 EGTA, 4 MgATP, 0.5 NaGTP, and 10 phosphocreatine to assess membrane properties and glutamatergic events. A cesium-based internal solution (290 mOsm/L), pH 7.24, containing the following (in mM), 128 CsMS, 11 KCl, 10 HEPES,

0.1 $CaCl_2$, 1 EGTA, 4 MgATP, and 0.5 NaGTP, was used to record GABAergic events. Voltage-clamp recordings were acquired at a holding potential of $V_h = -60$ and -5 mV for excitatory and inhibitory events, respectively, using a MultiClamp 700B amplifier (Molecular Devices) and digitized using a Digidata 1440A (Molecular Devices). Biocytin (0.4%; Cayman Chemical) was added to the internal solution for post hoc thick tissue IHC in a subset of recorded cells. Traces were acquired at 10 kHz and low-pass filtered at 3 kHz by pClamp 10.3 or 11 software (Molecular Devices), as previously described (Chee et al., 2010).

Drug application. Pharmacological applications of MCH (H-1482, Bachem) was applied by bath perfusion or puff application after a baseline period of at least 5 or 1 min, respectively, where the membrane potential fluctuated by <10%. Cells were held for at least 20 min during the MCH washout period to assess the reversibility of MCH-mediated effects on the membrane potential. Where applicable, tetrodotoxin (TTX) citrate (500 nM; T-550, Alomone Labs) or the MCHR1 antagonist TC-MCH 7c (10 µM; 4365, Tocris Bioscience) was bath applied and allowed to saturate the slice for at least 10 min prior to MCH application and then maintained during the MCH application and washout period as well.

Puff-applied MCH was delivered via a puff pipette backfilled with 3 µM MCH (or bath ACSF) positioned within 20–40 µm away from the patched cell held in the whole-cell configuration. A short "puff" was applied by manually applying positive pressure via the puff pipette, and a solution ripple can be seen to contact the patched cell.

Experimental design and statistical analyses

qPCR studies. Comparisons of *Mchr1* gene expression in WT mice ($N = 6–7$/sex) were analyzed using a between-subject design. *Mchr1* expressions in different regions were analyzed using a two-way mixed–model ANOVA with Šidák post hoc testing to determine sex differences.

Neuroanatomical studies. Comparisons of the total number of MCHR1-expressing cells were analyzed using a between-subject design from ($N = 3$/sex) and compared via unpaired t test, and differences in the distribution of MCHR1-expressing cells across each *ARA* level between sexes were determined by the two-way mixed–model ANOVA.

Comparisons of *Mchr1-*, *Vglut2-*, *Vgat-*, or TH-expressing cells were analyzed from male and female WT mice ($N = 6$) using a between-subject design, and a one-way ANOVA was used to identify distinct VTA cell groups. Sex differences were determined by two-way ANOVA.

Electrophysiological studies. Acute brain slices were prepared from male and female *Th-cre;L10-Egfp* ($N = 27$), *Vgat-cre;L10-Egfp* ($N = 8$), and *Vglut2-cre;L10-Egfp* ($N = 8$) reporter mice. Up to three cells were recorded from three to four coronal slices, where the VTA sits between the medial mammillary nucleus and compact part of the substantia nigra in rostral sections and sits beside the interpeduncular nucleus in caudal sections. Recordings from EGFP-labeled VTA cells of each reporter line were guided by atlas maps of *Mchr1* expression in each cell type. Electrical signals recorded were processed in Clampfit 10.7 (Molecular Devices).

The resting membrane potential (RMP) was sampled every 1 s and averaged into 30 s bins in bath-applied treatments and sampled every 100 ms and averaged into 1 s bins in puff-applied treatments. Cells deemed to be MCH-responsive exhibited a change in RMP (Δ RMP) lasting at least 2 min that was greater than two times the standard deviation of the mean RMP at the baseline. MCH-mediated Δ RMP was sampled within 7 min after MCH application or within 5 s of puff application. Comparisons of mean RMP before and after MCH application were determined via a paired t test and reported with effect size (η^2). Comparisons of MCH-mediated Δ RMP over time in the presence or absence of TTX were determined using within-subject design and repeated-measure two–way ANOVA with Šidák post hoc testing.

Excitatory (EPSC) and inhibitory postsynaptic current (IPSC) events were detected using MiniAnalysis (Synaptosoft). The event detection threshold was set to five times the root mean square noise level for each recording. The frequencies of EPSCs and IPSCs were indirectly determined by the interevent interval between events using

MiniAnalysis (Synaptosoft) and averaged into 30 s bins. The baseline event frequency or amplitude was determined as the mean event frequency averaged over 5 min immediately prior to MCH bath application. Comparisons of mean event frequency or amplitude before and after MCH application were determined via a paired t test and reported with effect size (η^2). Comparisons of MCH-mediated effects on postsynaptic current events over time in the presence or absence of TTX or TC-MCH 7c were determined using the within-subject design and repeated-measure two–way ANOVA with Šidák post hoc testing.

Graphs. Only responders were included in our graphical representations, unless a null response was referenced. All data graphs were prepared using Prism 9 (GraphPad Software). Results were considered statistically significant at $p < 0.05$. All data are reported as group mean ± SEM. Figures were assembled in Adobe Illustrator 2020 (Adobe). Numerals in parentheses in graphs represent the number of animals (N) or cells (n).

Results

Moderate *Mchr1* mRNA and MCHR1 protein expression in the mouse VTA

Mchr1 mRNA and protein have been reported in the rat VTA (Hervieu et al., 2000; Saito et al., 2001), and we first determined *Mchr1* mRNA and/or protein expression in the VTA of male and female WT mice. While the level of *Mchr1* mRNA varied across brain regions ($F_{(4, 44)} = 81.6$; $p < 0.0001$; ANOVA), it was similar between male and female mice ($F_{(1, 11)} = 0.6$; $p = 0.449$; ANOVA), and there was no interaction between brain region and sex ($F_{(4, 44)} = 0.8$; $p = 0.561$; ANOVA). As expected, *Mchr1* expression was highest in the striatum, which included the nucleus accumbens and caudate putamen, and barely detectable in the cerebellum (Fig. 1A). Importantly, *Mchr1* expression in the VTA was comparable to the hypothalamus (male, $t_{(44)} = 1.5$; $p = 1.000$; female, $t_{(44)} = 1.0$; $p = 1.000$) and hippocampus (male, $t_{(44)} = 1.3$; $p = 1.000$; female, $t_{(44)} = 0.6$; $p = 1.000$; Fig. 1A).

The VTA of WT male and female mice also comprised MCHR1-ir signals, which appeared long and spindle-like and were consistent with MCHR1 expression observed on the primary cilium of neurons (Fig. 1B). No MCHR1-ir labeling was detected in the VTA of *Mchr1-KO* mice (Fig. 1C). Male and female WT mice had a similar distribution pattern of MCHR1-expressing cells throughout the VTA ($F_{(1, 4)} = 0.02$; $p = 0.891$; ANOVA; Fig. 1D). Additionally, there was no difference in the total number of MCHR1-expressing cells in the VTA of male (159 ± 48; $n = 3$) and female (171 ± 29; $n = 3$) mice ($t_{(4)} = 0.2$; $p = 0.835$; $\eta^2 = 0.01$; unpaired t test).

Neurochemical diversity of VTA cells

The VTA comprises multiple cell types, including dopaminergic, GABAergic, or glutamatergic cells that have distinct distribution patterns (Morales and Root, 2014; Morales and Margolis, 2017). To identify the neurochemical identities of VTA cell types, we determined if *Mchr1* hybridization colocalized with *Vglut2* or *Vgat* hybridization in glutamatergic or GABAergic cells, respectively, or with TH immunoreactivity in dopaminergic cells within the same tissue. As there were no sex differences in *Mchr1* mRNA (Fig. 1A) or protein expression (Fig. 1D), we herein combined our neuroanatomical analyses from male and female mice.

The overall number of VTA cells labeled by *Vglut2* mRNA, *Vgat* mRNA, and/or TH immunoreactivity decreased posteriorly (Fig. 2A, gray line). We compared the distribution of *Vglut2* mRNA, *Vgat* mRNA, and TH-ir cells within the VTA to determine their relative prevalence rostrocaudally, and we distinguished at least five subtypes of VTA cells ($F_{(4, 50)} = 13.4$; $p = 0.0001$;

ANOVA). *Vglut2* cells were most prominent anteriorly and then gradually diminished toward the posterior VTA (Fig. 2A), and they were usually medially distributed within the VTA (Fig. 2B). *Vgat* cells comprised ~30% of VTA cells counted through the anterior and middle sections of the VTA (L80–87) but made up the majority of cells in the posterior VTA (L88–90; Fig. 2A). TH-ir cells were most numerous in the middle of the VTA and comprised ~40% of cells counted (Fig. 2A). Both *Vgat* and TH cells tended to be laterally distributed, though some *Vgat* cells were spread medially (Fig. 2B).

In addition, we also found that VTA cells may express two or more neurotransmitter markers. The most common were those expressing both *Vglut2* and *Vgat* that comprised 5–10% of VTA cells and up to 16% of cells toward the middle of the VTA (L86–87; Fig. 2A). Cells expressing TH and *Vglut2* emerged toward the posterior VTA (L85–89) but comprised <6% at its peak (Fig. 2A) so were not mapped. Similarly, just 0.25% of cells exhibited TH and *Vgat*, and cells exhibiting *Vglut2*, *Vgat*, and TH were even rarer (<0.05%; data not shown).

Neurochemical and spatial distribution of *Mchr1* mRNA expression in the VTA

Mchr1 mRNA expression was widely distributed throughout the VTA (Fig. 3A) and across all major VTA cell types (Fig. 3B–E). Consistent with the rostrocaudal composition of VTA cells, *Mchr1* expression was predominantly in *Vglut2* cells rostrally, TH cells in the middle sections of the VTA, and *Vgat* cells caudally (Fig. 3F). Interestingly, some *Mchr1* cells (*Mchr1*-only) are yet to be defined neurochemically as they do not coexpress TH, *Vglut2*, or *Vgat*, and these *Mchr1*-only cells can be seen throughout the VTA (Fig. 3F). There was no sex difference in the heterogeneity of *Mchr1* VTA cells ($F_{(1, 24)} = 0.01$; $p = 0.924$; ANOVA; Fig. 3G), but *Mchr1*-only cells tend to be less prominent in the VTA of female mice, as sex may interact with *Vgat* expression in *Mchr1* cells ($F_{(1, 8)} = 4.8$; $p = 0.059$; ANOVA; Fig. 3H).

About half (52%) of *Vglut2* VTA cells expressed *Mchr1* mRNA (Fig. 4Ai), which was evenly distributed throughout *Vglut2* cells in the medial and anterior VTA (Fig. 4Aii–iv) but only sparsely distributed posteriorly (Fig. 4Avi–viii). In contrast, few *Vgat* cells in the anterior VTA expressed *Mchr1* mRNA (Fig. 4Bi–iii), but in the middle and posterior VTA sections where *Mchr1*-expressing *Vgat* cells were more common, they tend to be laterally distributed or have no discernible pattern, respectively (Fig. 4Bv–viii). Interestingly, the majority of TH-ir VTA neurons (78%) expressed *Mchr1* mRNA (Fig. 4Ci), and while *Mchr1*-expressing TH cells were found sparingly in the anterior VTA (Fig. 4Cii,iii), they were abundant in middle VTA sections, especially near the ventral and lateral borders of the VTA (Fig. 4Civ–vi). In addition, although dual *Vglut2* and *Vgat* cells comprised just 1/10 of all VTA cells, nearly 60% of them expressed *Mchr1* mRNA (Fig. 4Di) and were most likely found in the dorsomedial aspects of the VTA (Fig. 4Dv,vi). Taken together, these findings indicated the abundance of *Mchr1* mRNA throughout the VTA in glutamatergic, GABAergic, and/or dopaminergic VTA cells.

MCH inhibited *Vgat* and *Th* VTA cells but not *Vglut2* VTA cells

Based on the spatial distribution of *Mchr1* expression in *Vglut2*, *Vgat*, and TH VTA cells (Fig. 4), we performed whole-cell patch–clamp recordings in EGFP-labeled *Vglut2*^{EGFP}, *Vgat*^{EGFP}, and *Th*^{EGFP} VTA cells from *Vglut2-cre;L10-Egfp* (Fig. 5Ai),
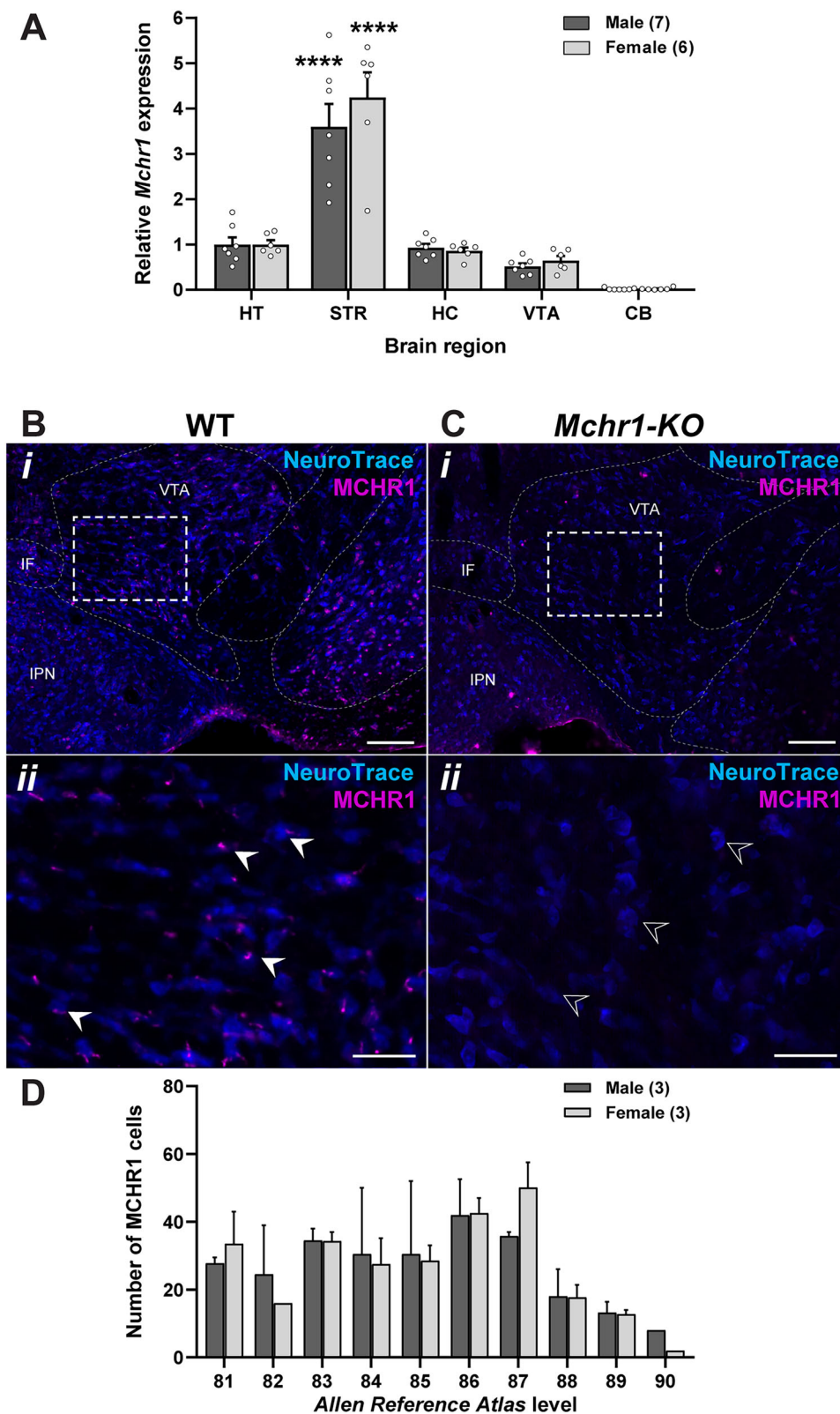
Figure 1. *Mchr1* mRNA and MCHR1 protein expression in WT mouse VTA. qPCR analysis of *Mchr1* mRNA from the hypothalamus (HT), striatum (STR), hippocampus (HC), VTA, and cerebellum (CB) of male and female WT mice (***A***). Confocal photomicrographs of MCHR1-ir signals on Nissl-stained (NeuroTrace) soma in WT (***B***) and *Mchr1-KO* (***C***) VTA at low (***i***) and high magnification (***ii***, from dash-outlined region in ***i***). Representative examples of the presence (white arrowhead) or absence (open arrowhead) of MCHR1 immunoreactivity at the primary cilium of VTA cells. The number of MCHR1-immunoreactive cells throughout the VTA of male and female WT mice (***D***). VTA levels were assigned with reference to the *ARA* (*ARA*; Dong, 2008). Two-way ANOVA with Bonferroni's post-test: ****$p < 0.0001$ (STR vs all regions; ***A***). Scale bars: ***i***, 100 μm; ***ii***, 40 μm. IF, interfascicular nucleus raphe; IPN, interpeduncular nucleus; VTA, ventral tegmental area.
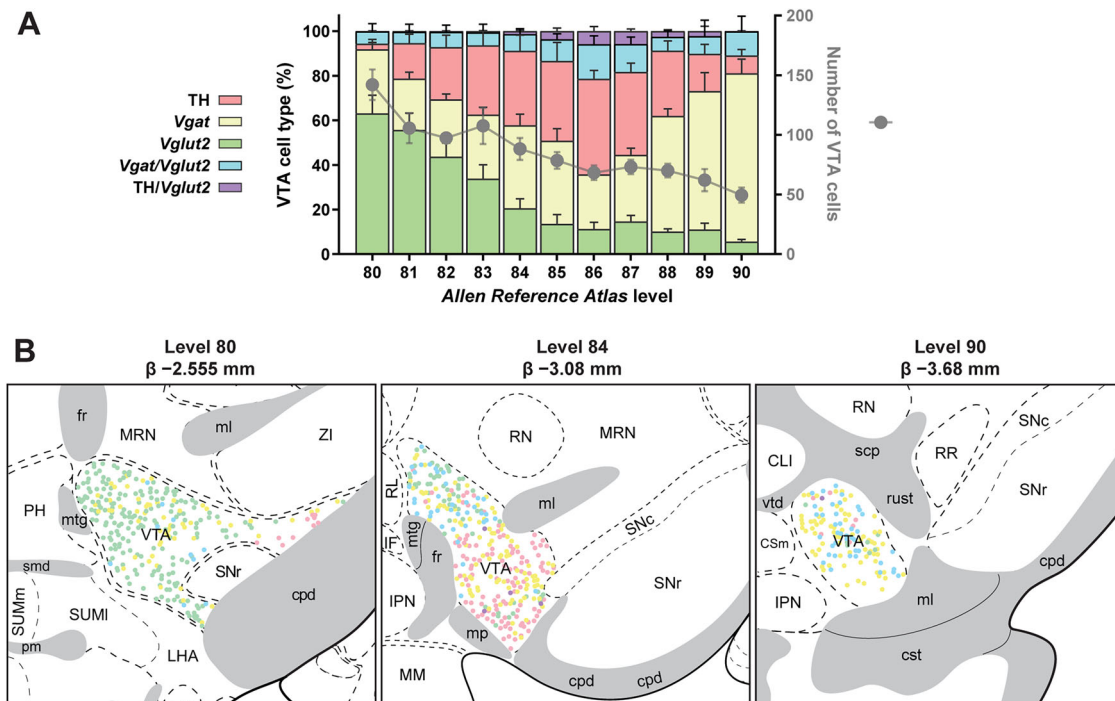
Figure 2. Neurochemical characterization of VTA cells. The number (right *y*-axis, gray line) and proportion of each cell type (left *y*-axis, stacked colored bars) at each *ARA* level (Dong, 2008) rostrocaudally from VTA slices expressing *Vglut2* mRNA hybridization, *Vgat* mRNA hybridization, and TH immunoreactivity (*N* = 6 mice; ***A***). Representative coronal brain maps of VTA cells that are *Vglut2*-, *Vgat*-, and/or TH-positive (***B***). Each panel includes the nomenclature, atlas level, and bregma value (*β*) assigned to that tissue in accordance with the *ARA* (Dong, 2008).

Vgat-cre;L10-Egfp (Fig. 5*Bi*), and *Th-cre;L10-Egfp* reporter mice (Fig. 5*Ci*), respectively. MCH (3 μM) bath application had no effect on the RMP (baseline, −59.6 ± 3.2 mV; MCH, −59.7 ± 3.8 mV; *n* = 6 cells; $t_{(5)} = 0.20$; *p* = 0.849; $\eta^2 = 0.01$; paired *t* test) of $Vglut2^{EGFP}$ VTA cells (*n* = 0/6 cells; *N* = 3; Fig. 5*Aii*). In contrast, MCH hyperpolarized $Vgat^{EGFP}$ (baseline, −47.8 ± 1.9 mV; MCH, −49.9 ± 1.7 mV; *n* = 6/15 cells; *N* = 6; $t_{(5)} = 3.70$; *p* = 0.014; $\eta^2 = 0.73$; paired *t* test; Fig. 5*Bii*) and Th^{EGFP} cells (baseline, −53.5 ± 3.6 mV; MCH, −57.8 ± 2.8 mV; *n* = 6/16 cells; *N* = 12; $t_{(5)} = 3.15$; *p* = 0.025; $\eta^2 = 0.66$; paired *t* test; Fig. 5*Cii*) within 10 min and persisted for at least 25 min before gradually returning to the baseline.

While the proportion of MCH-sensitive $Vgat^{EGFP}$ VTA cells could be predicted by the availability of *Mchr1* expression at *Vgat* cells (Fig. 4*B*), the proportion of MCH-sensitive Th^{EGFP} cells was lower than predicted by the prevalence of *Mchr1* expression at TH-ir cells (Fig. 4*C*). We first confirmed that over 80% (*n* = 13/16 cells; *N* = 7) of Th^{EGFP} cells in patch-clamp recordings expressed TH immunoreactivity (Fig. 6*A*). We then determined the proportion of TH-ir cells that expressed MCHR1 protein (Fig. 6*B*). Interestingly, only about one-third of TH-ir cells within the span of the VTA targeted for patch-clamp recordings (L84–87) expressed MCHR1 (Fig. 6*C*), which is comparable with a lower (38%) proportion of MCH-sensitive Th^{EGFP} cells surveyed by patch-clamp recordings (Fig. 5*Cii*).

We then assessed if MCH-mediated inhibition of $Vgat^{EGFP}$ and Th^{EGFP} VTA cells was activity-dependent by pretreatment with the voltage-gated sodium channel blocker TTX. Since the effect of bath-applied MCH was so long-lasting, we first established if MCH-sensitive VTA cells could be identified by a short puff application of MCH (Fig. 7*Ai*) lasting <5 s to allow rapid recovery of the RMP (Fig. 7*Aii*). A single puff of MCH produced an acute membrane hyperpolarization (baseline, −55.5 ± 4.2 mV; Δ RMP, −6.7 ± 1.8 mV; *n* = 4) that peaked within 10 s and

returned to the baseline within 1 min. A second puff of MCH applied 3–5 min later at the same cell elicited a similar hyperpolarization (baseline, −55.9 ± 4.3 mV; Δ RMP, −4.3 ± 1.7 mV; *n* = 4) and time course ($F_{(1, 6)} = 3.3$; *p* = 0.120; ANOVA; Fig. 7*Aiii*). Importantly, puff application of ACSF produced visibly different outcomes than the first MCH puff ($F_{(1, 5)} = 6.8$; *p* = 0.047; ANOVA) or second MCH puff ($F_{(1, 5)} = 30.7$; *p* = 0.003; ANOVA), as ACSF application did not effect changes in membrane potential (baseline, −56.3 ± 2.7 mV; Δ RMP, −0.2 ± 0.6 mV; *n* = 3; Fig. 7*Aiii*). This thus showed that a localized MCH puff could identify MCH-sensitive VTA cells by enabling short-lived but reproducible membrane hyperpolarizations that were not significantly desensitized by repeated application.

We then puff-applied MCH to identify MCH-sensitive $Vgat^{EGFP}$ and Th^{EGFP} VTA cells and compared the effect of MCH before and after TTX (500 nM) treatment. About two-thirds of *n* = 10/15 of $Vgat^{EGFP}$ cells were "nonresponders" and whose RMP was unaltered by puffed MCH (baseline, −59.8 ± 1.4 mV; Δ RMP, −0.03 ± 0.19 mV; *n* = 10; $F_{(1, 14)} = 4.9$; *p* = 0.043; mixed-effect analysis; Fig. 7*B*). MCH-mediated hyperpolarization at $Vgat^{EGFP}$ VTA cells (baseline, −56.6 ± 1.3 mV; Δ RMP, −1.5 ± 0.5 mV; *n* = 5) persisted in the presence of TTX (baseline, −55.2 ± 1.3 mV; Δ RMP, −1.1 ± 0.4 mV; *n* = 4) over time ($F_{(1, 7)} = 0.03$; *p* = 0.869; mixed-effect analysis; Fig. 7*B*). Similarly, Th^{EGFP} VTA cells also remained sensitive to the peak effect of MCH (baseline, −57.1 ± 3.6 mV; Δ RMP, −5.4 ± 1.6 mV; *n* = 5) in the presence of TTX (baseline, −50.1 ± 3.4 mV; Δ RMP, −4.3 ± 1.0 mV; *n* = 5) and over time ($F_{(1, 8)} = 0.3$; *p* = 0.623; ANOVA; Fig. 7*C*). However, nonresponsive Th^{EGFP} cells were also common (baseline, −56.9 ± 2.3 mV; Δ RMP, −0.3 ± 0.3 mV; *n* = 7/12; $F_{(1, 10)} = 7.7$; *p* = 0.020; mixed-effect analysis; Fig. 7*C*). These findings indicated that MCH directly hyperpolarized $Vgat^{EGFP}$ and Th^{EGFP} VTA cells.
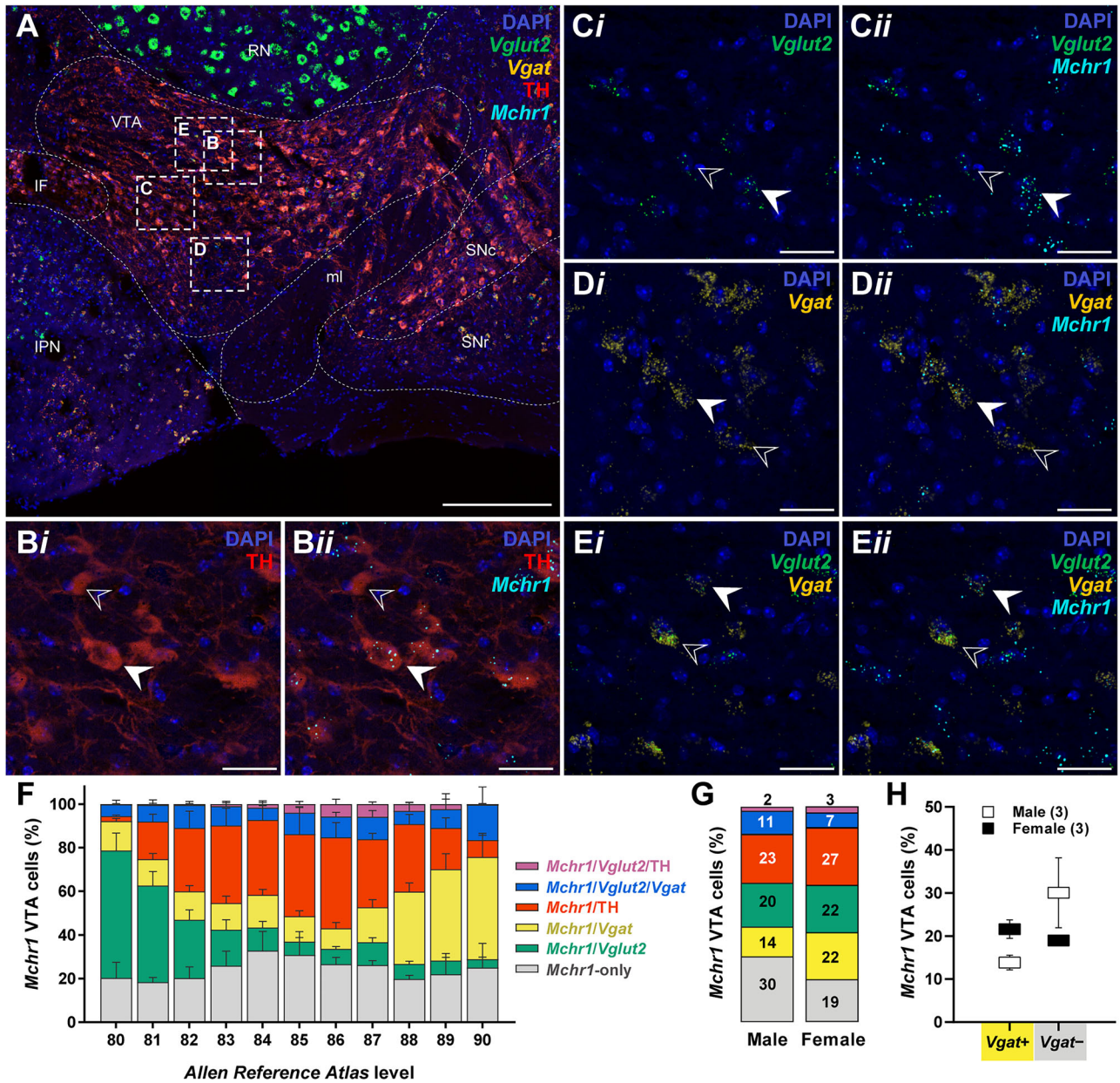
Figure 3. *Mchr1* expression on diverse VTA cell types. Representative low- (**A**) and high-magnification confocal photomicrographs (**B–E**), from corresponding dash-outlined region in **A** of *Vglut2* mRNA, *Vgat* mRNA, and/or TH immunoreactivity (**i**) that coexpress (white arrowhead) or lack (open arrowhead) *Mchr1* mRNA hybridization in VTA cells (**ii**). Relative proportion of *Mchr1*-expressing VTA cells at each level, as determined with reference to the *ARA* (Dong, 2008), of the VTA ($N = 6$; **F**). Relative distribution of *Mchr1*-expressing VTA cells (**G**) and comparison of *Mchr1*-only and *Mchr1*/*Vgat* VTA cells in male and female mice (**H**). Scale bars: **A**, 250 μm; **B–E**, 30 μm. IF, interfascicular nucleus raphe; IPN, interpeduncular nucleus; ml, medial lemniscus; RN, red nucleus; SNc, substantia nigra, compact part; SNr, substantia nigra, reticular part; VTA, ventral tegmental area.

MCH increased glutamatergic input to *Th* VTA cells

Dopaminergic output from the VTA can be regulated by local glutamatergic and GABAergic circuitry (Wang et al., 2015; Bariselli et al., 2016; Morales and Margolis, 2017); thus, we assessed if MCH regulated the GABAergic and/or glutamatergic input to Th^{EGFP} VTA cells. Bath application of MCH did not alter the frequency (baseline, 0.9 ± 0.1 Hz; MCH, 0.9 ± 0.1 Hz; $n = 9$; $t_{(8)} = 0.33$; $p = 0.750$; $\eta^2 = 0.01$; paired t test; Fig. 8A,B) or amplitude (baseline, 13.1 ± 0.8 pA; MCH, 13.4 ± 0.8 pA; $n = 9$; $t_{(8)} = 0.60$; $p = 0.563$; $\eta^2 = 0.04$; paired t test; Fig. 8C) of spontaneous IPSC (sIPSC) events arriving at Th^{EGFP} VTA cells.

Interestingly, MCH elicited a delayed increase in baseline spontaneous EPSC (sEPSC) frequency (1.3 ± 0.4 Hz, $n = 8$) at

Th^{EGFP} VTA cells that gradually peaked ∼25 min following MCH application (Fig. 8D). To determine if this delayed sEPSC frequency increase was MCH-dependent, we tracked the change in sEPSC frequency in the absence of MCH (ACSF only) or in the presence of a MCHR1 antagonist, TC-MCH 7c. Following MCH treatment, sEPSC frequency increased from 1.3 ± 0.4 Hz to 2.6 ± 0.6 ($n = 8$; $t_{(7)} = 3.17$; $p = 0.016$; $\eta^2 = 0.59$; paired t test), which was not seen when bathed in ACSF only (baseline, 1.0 ± 0.4 Hz; MCH, 0.9 ± 0.5 Hz; $n = 4$; $t_{(3)} = 0.34$; $p = 0.760$; $\eta^2 = 0.03$; paired t test). The MCH-mediated increase in sEPSC frequency was also not seen when MCH was applied in the presence of TC-MCH 7c (baseline, 0.9 ± 0.4 Hz; MCH in TC-MCH 7c, 0.8 ± 0.3 Hz; $n = 7$; $t_{(6)} = 0.29$; $p = 0.780$; $\eta^2 = 0.01$;
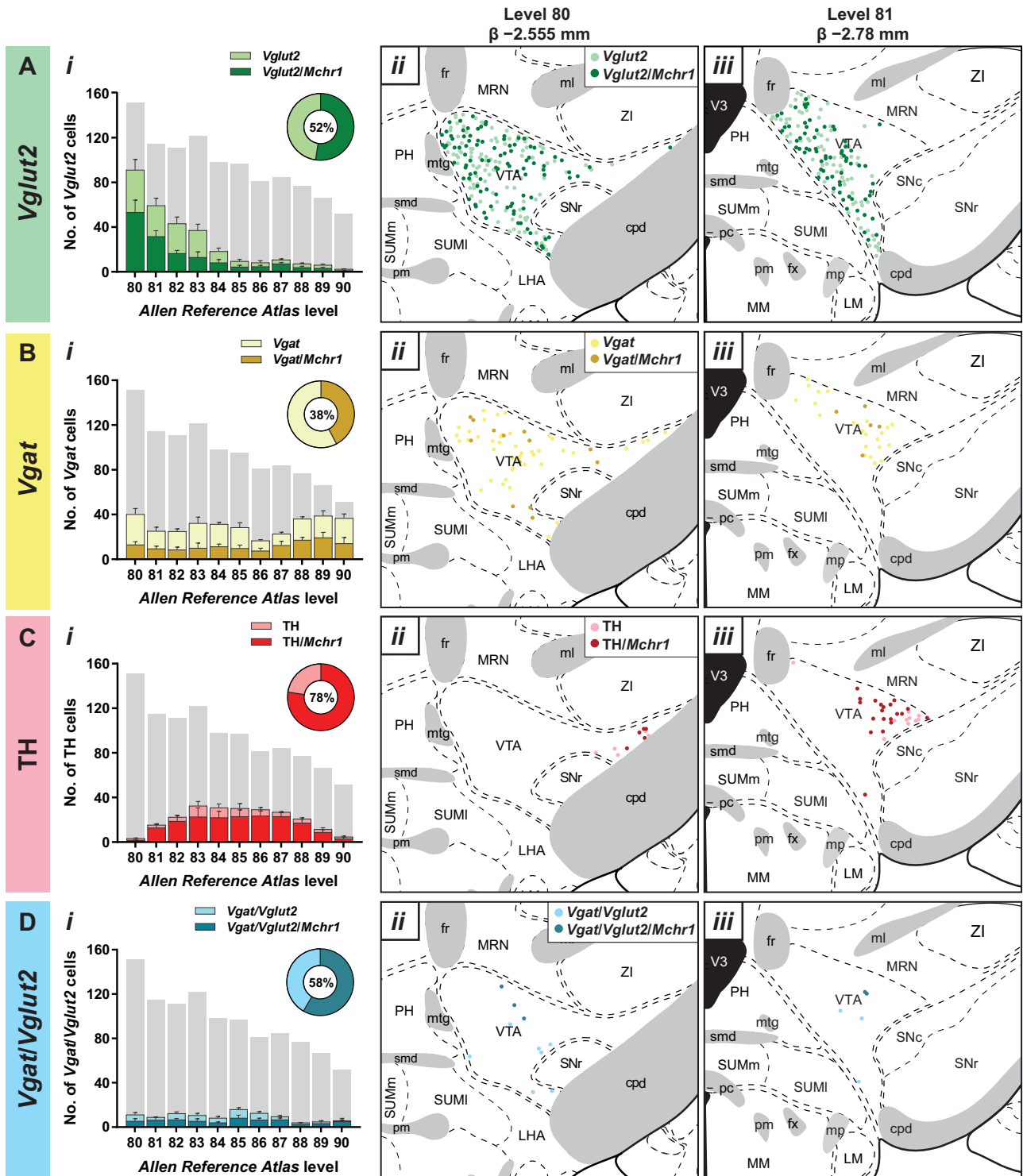
Figure 4. Spatial distribution of *Mchr1* mRNA in heterogeneous VTA cells. The number (*N* = 6; ***i***) and distribution (***ii–viii***) of *Mchr1*-positive (dark) or *Mchr1*-negative (light) *Vglut2* (***A***), *Vgat* (***B***), TH (***C***), or dual *Vglut2* and *Vgat* VTA cells (***D***) mapped throughout the VTA using *ARA* (Dong, 2008) templates. Each panel includes the nomenclature, atlas level, and bregma value (*β*) indicated (top). (*Figure continues.*)

paired *t* test). There was a main effect of drug over time ($F_{(2, 16)}$ = 4.6; $p = 0.027$; ANOVA; Fig. 8*Ei*), as the time course of fold change in sEPSC frequency with MCH treatment was significantly different than in ACSF ($t_{(16)} = 2.6$; $p = 0.036$; Šidák post-test; Fig. 8*Ei*) or when MCH was applied in the presence of TC-MCH 7c ($t_{(15)} = 2.4$; $p = 0.058$; Šidák post-test; Fig. 8*Ei*). This difference was largely attributed to a delayed increase in

sEPSC frequency that was prominent >20 min after drug treatment. Overall, the average fold change in sEPSC frequency in MCH (2.8 ± 0.6, $n = 8$) was significantly greater than in ACSF only (0.8 ± 0.2; $n = 4$; $t_{(16)} = 2.93$; $p = 0.029$; ANOVA) or when applied at Th^{EGFP} VTA cells pretreated with TC-MCH 7c (0.8 ± 0.1; $n = 7$; $t_{(16)} = 3.33$; $p = 0.013$; ANOVA; Fig. 8*Eii*). There was no main effect of MCH on sEPSC amplitudes over
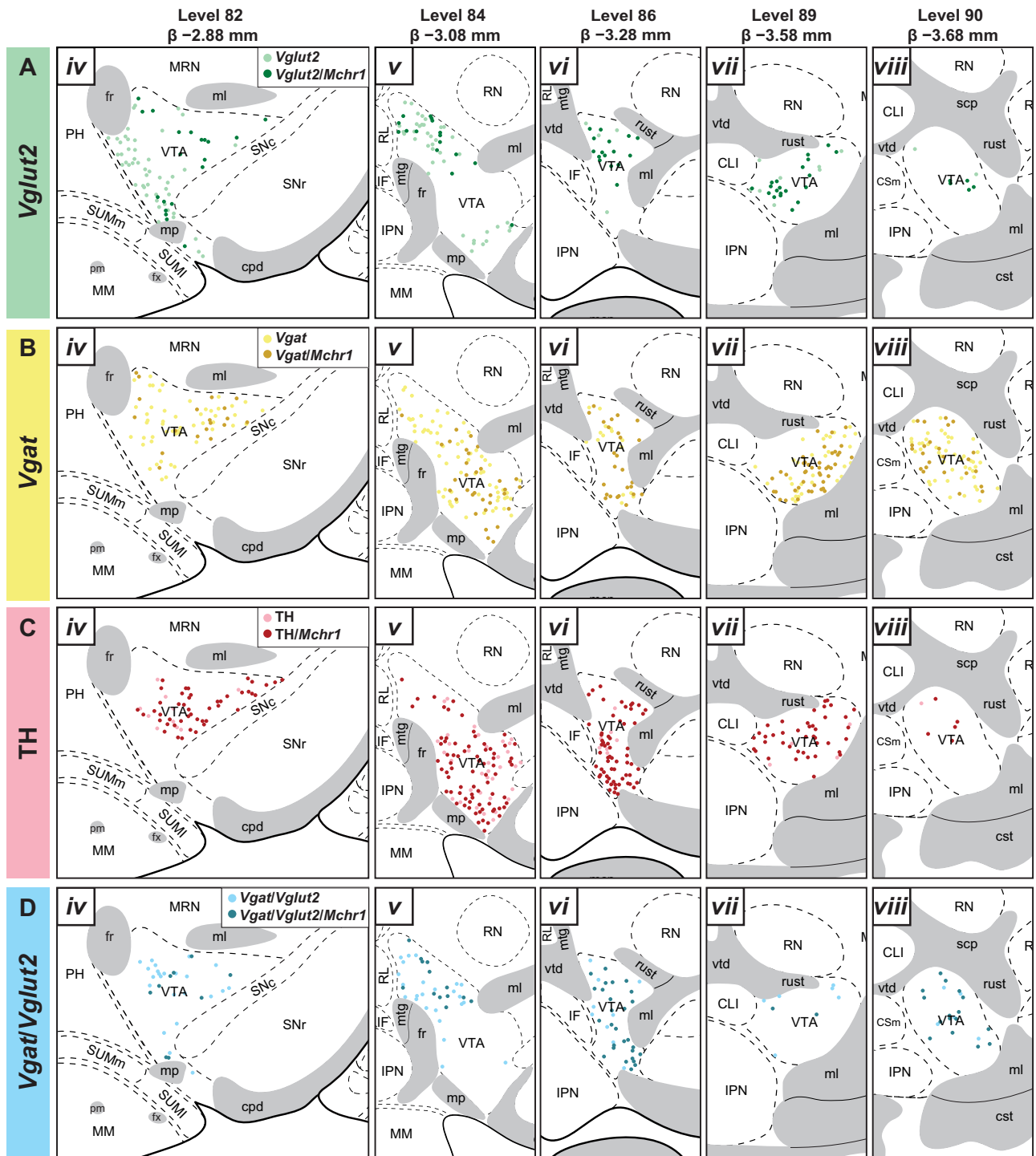
Figure 4. Continued

time ($F_{(2, 16)} = 2.3$; $p = 0.130$; ANOVA; Fig. 8Fi) or when comparing their fold change within each condition ($F_{(2, 16)} = 0.18$; $p = 0.176$; one-way ANOVA; Fig. 8Fii).

To determine the role of upstream targets that facilitate excitatory input to Th^{EGFP} VTA cells, we isolated the presynaptic excitatory input (miniature EPSC, mEPSC) with TTX pretreatment (Fig. 9A). MCH-mediated glutamate release at Th^{EGFP} VTA cells was largely abolished in the presence of TTX (Fig. 9B). However, a slight 1.5 ± 0.4-fold (baseline, 1.2 ± 0.5 Hz; MCH, 1.5 ± 0.6 Hz; $n = 6$; $t_{(5)} = 2.27$; $p = 0.072$; $\eta^2 = 0.51$;

paired t test) increase in mEPSC frequency can be detected at some Th^{EGFP} VTA (Fig. 9B); thus, it is possible that MCH mediated glutamate release directly at glutamatergic terminals. There was no change in mEPSC amplitude following MCH treatment (baseline, 14.9 ± 1.9 pA; MCH, 14.9 ± 1.7 pA; $n = 6$; $t_{(5)} = 0.05$; $p = 0.961$; $\eta^2 = 0.001$; paired t test) or over time (Fig. 9C). We thus considered that MCH may recruit upstream targets that indirectly regulate the excitatory input at Th^{EGFP} VTA cells.

As MCHR1 is a known inhibitory $G_{i/o}$-protein–coupled receptor (Hawes et al., 2000), we determined if the
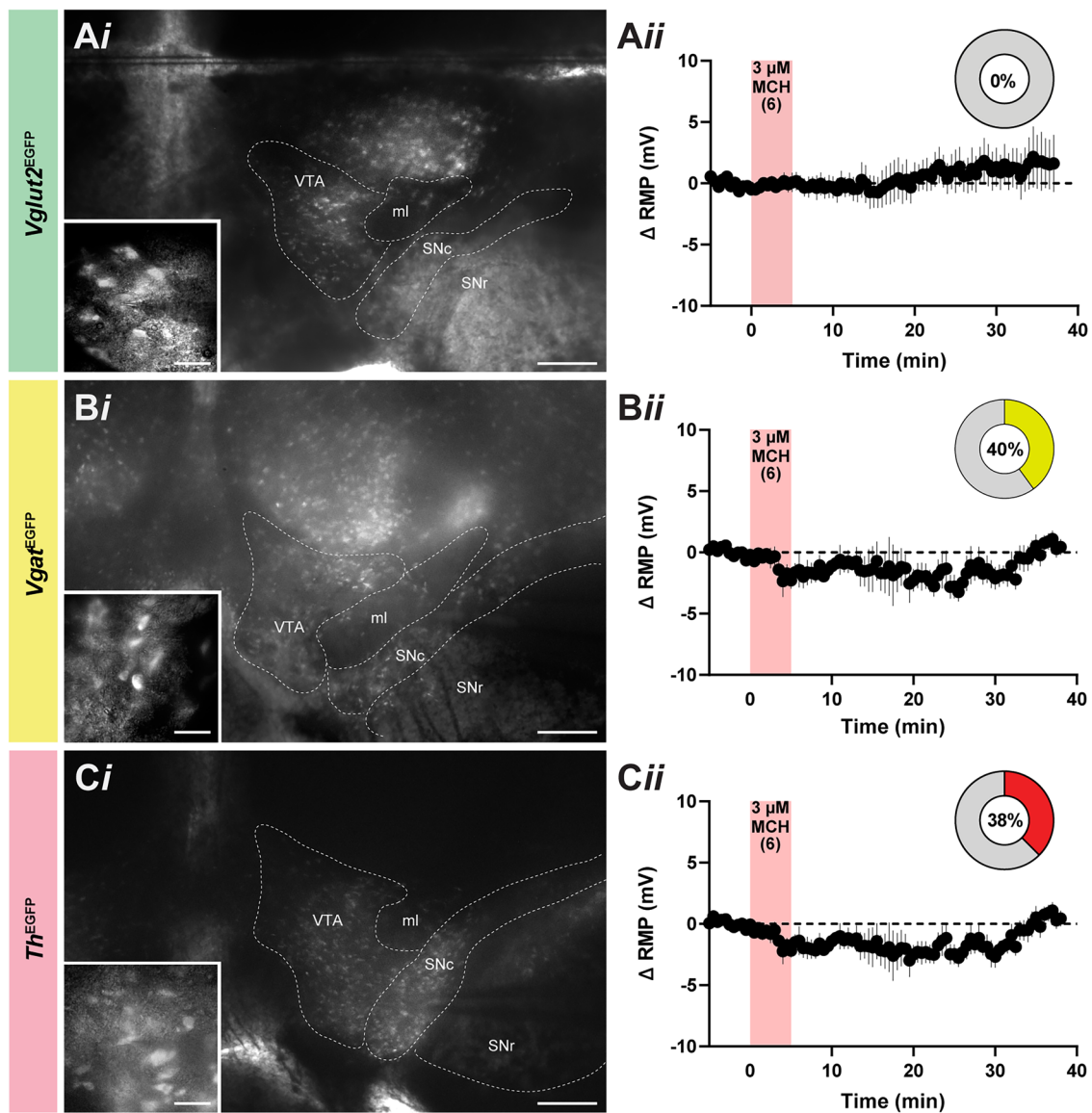
Figure 5. MCH hyperpolarized GABAergic and dopaminergic VTA cells. Representative epifluorescence image of coronal VTA brain slices (*i*) where cells expressing native EGFP fluorescence (inset in *i*) from *Vglut2-cre;L10-Egfp* (**A**), *Vgat-cre;L10-Egfp* (**B**), and *Th-cre;L10-Egfp* reporter mice (**C**) guided whole-cell patch–clamp recordings to determine the Δ RMP over time following the bath application of 3 μM MCH (*ii*) and proportion of MCH-responsive cells (donut plot in *ii*). Scale bars: **i**, 250 μm; *inset* in **i**, 20 μm. ml, medial lemniscus; SNc, substantia nigra, compact part; SNr, substantia nigra, reticular part; VTA, ventral tegmental area.

MCH-mediated increase in the glutamatergic tone at Th^{EGFP} VTA cells may be ascribed to GABAergic disinhibition at glutamatergic nerve terminals (Fig. 9D). We recorded from $Vglut2^{EGFP}$ VTA cells and found that MCH produced a prolonged 0.4 ± 0.1-fold decrease in sIPSC frequency (baseline, 1.7 ± 0.4 Hz; MCH, 1.0 ± 0.3 Hz; $n = 5$; $t_{(4)} = 5.08$; $p = 0.007$; $\eta^2 = 0.87$; paired t test; Fig. 9E) but not amplitude of sIPSC events (baseline, 14.4 ± 1.3 pA; MCH, 19.3 ± 5.0 pA; $n = 5$; $t_{(4)} = 0.95$; $p = 0.395$; $\eta^2 = 0.19$; paired t test; Fig. 9F). Overall, these recordings suggested that, in addition to directly inhibiting Th VTA cells, MCH may also engage a local disynaptic circuit from $Vgat$ and $Vglut2$ VTA cells to regulate the VTA output (Fig. 9G).
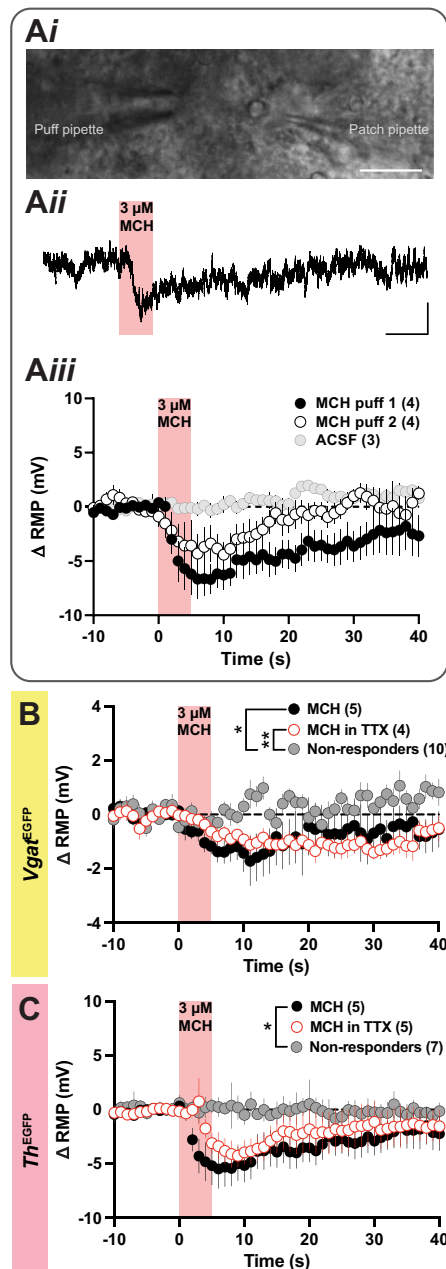
Discussion

MCH can directly and indirectly regulate Th VTA cells. MCHR1-expressing cells were widespread through the VTA,

including at glutamatergic *Vglut2*, GABAergic *Vgat*, and dopaminergic TH cells, thus providing a neuroanatomical basis for MCH action in the VTA. Electrophysiological recordings showed that MCH hyperpolarized and inhibited Th cells and $Vgat$ cells. Interestingly, MCH did not directly regulate $Vglut2$ cells but disinhibited $Vglut2$ afferents leading to increased excitatory transmission at Th cells. Therefore, functional MCHR1 activation in the VTA may provide bidirectional regulation of the dopamine output from the VTA.

The majority, nearly 80%, of TH-ir VTA cells expressed *Mchr1* mRNA, and MCH directly hyperpolarized 38% of Th VTA cells in an activity-independent manner, which is consistent with MCHR1 protein expression at TH-ir VTA cells. Furthermore, it is possible that native EGFP fluorescence may not reflect active TH cells, as Cre expression in TH-negative VTA cells may comprise up to half of all $EGFP^{Th}$ cells (Lammel et al., 2015). However, when patching within the
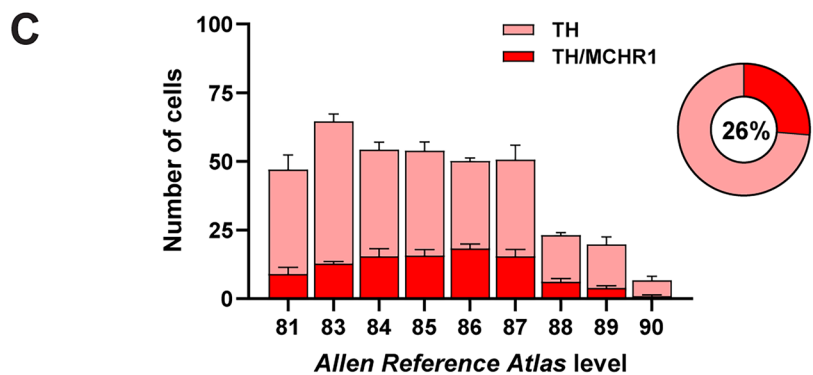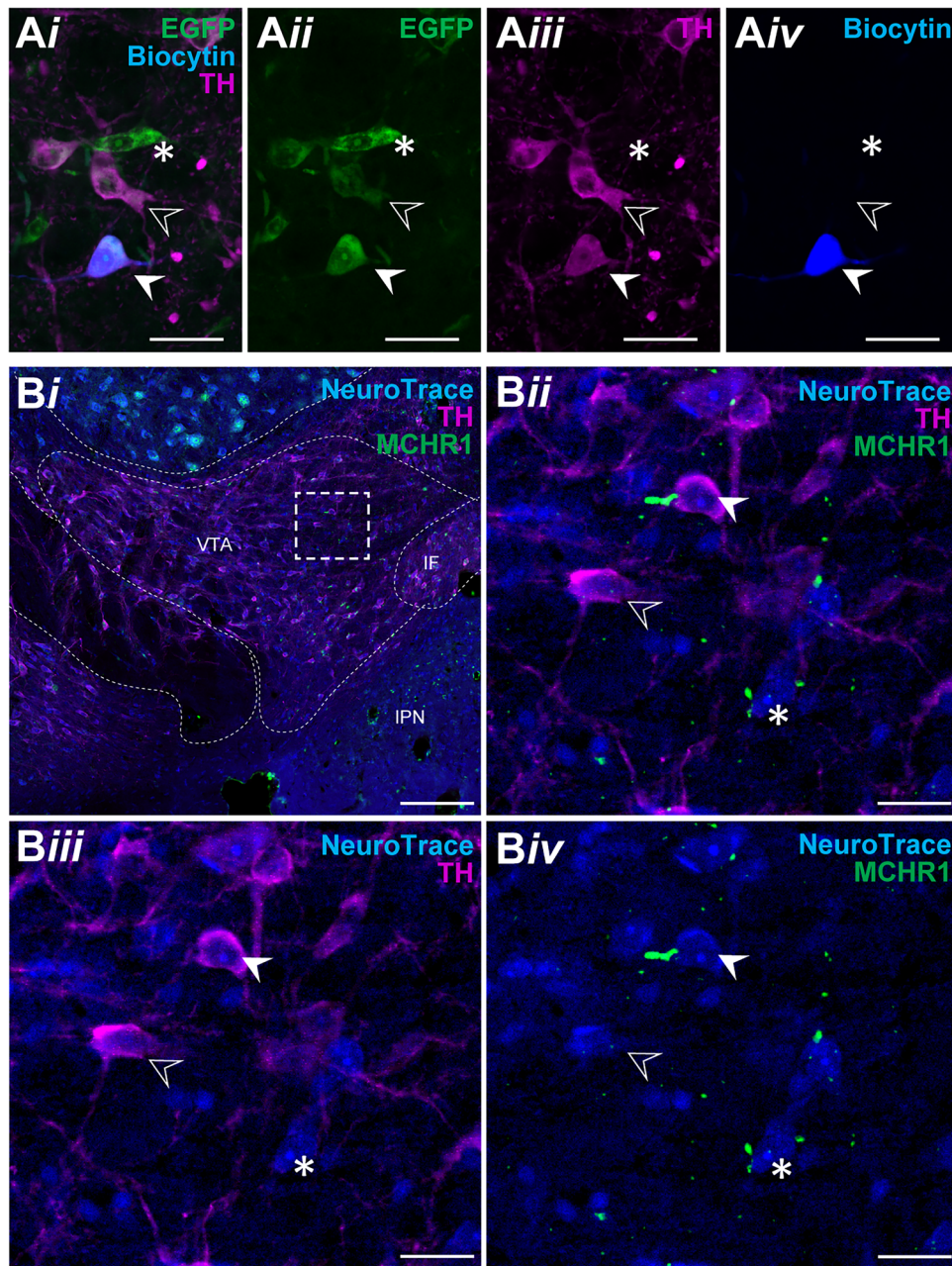
Figure 6. Selectivity of TH and MCHR1 coexpression in Th^EGFP VTA cells. Merged confocal photomicrograph (*i*) of native EGFP fluorescence (*ii*) and TH immunoreactivity (*iii*) in biocytin-filled (*iv*) cells from a subset of patch-clamp recordings from the VTA of *Th-cre;L10-Egfp* reporter mice (*A*). Merged confocal photomicrograph at low (*i*) and high magnification (*ii*, from dash-outlined region in *i*) of TH- (*iii*) and MCHR1-immunoreactive signals (*iv*) on Nissl-stained (NeuroTrace) soma in WT VTA (*B*). Representative examples of the presence (white arrowhead) or absence (open arrowhead) of MCHR1 immunoreactivity at the primary cilium of VTA TH cells or non-TH−labeled cells (*). Number and proportion (donut plot) of MCHR1-positive (red) or MCHR1-negative (pink) TH cells at each VTA level in accordance with the *ARA* (Dong, 2008) of male and female WT mice (*N* = 4; *C*). Scale bars: *A*, 30 μm; *Bi*, 200 μm; *Bii−iv*, 25 μm. IF, interfascicular nucleus raphe; IPN, interpeduncular nucleus; VTA, ventral tegmental area.

suppresses dopamine release (Chee et al., 2019). Furthermore, loss of MCH signaling increases accumbens dopamine accumulation leading to hyperactivity and increased energy expenditure (Pissios et al., 2008; Mul et al., 2011; Chee et al., 2019). As the main source of dopaminergic afferents to the accumbens arises from the VTA, it stands to reason that MCH may regulate dopamine release by direct inhibition of VTA neurons.

Interestingly, MCH action within the VTA caused a delayed increase in excitatory input to *Th* VTA cells. MCHR1 activation engages $G_{i/o}$- or G_q-protein systems (Pissios et al., 2003; Sears et al., 2010) to elicit inhibitory or excitatory actions, respectively. We considered that MCH may act presynaptically to stimulate glutamatergic afferents, but the MCH-mediated increase in glutamatergic transmission was abolished in the presence of TTX. This suggested that the stimulatory effect of MCH on glutamatergic afferents was indirect, activity-dependent, and polysynaptic. We thus examined if MCH may indirectly recruit glutamatergic afferents detected at *Th* VTA cells by suppressing the GABAergic input onto *Vglut2* VTA cells or axons. We found that MCH directly inhibited GABAergic VTA cells and suppressed the GABAergic input to *Vglut2* VTA cells. In effect, MCH can suppress GABAergic activity to disinhibit glutamatergic transmission at *Th* VTA cells, and we posit that this GABA-dependent microcircuit within the VTA may serve to restore the output of *Th* VTA cells that were acutely inhibited by MCH (Fig. 9G).

VTA *Vglut2* cells are known to innervate (Dobi et al., 2010) and regulate dopaminergic VTA cells (Wang et al., 2015; Bariselli et al., 2016). MCH had no effect on the membrane potential of *Vglut2* VTA cells. *Vglut2* cells were more abundant in the anterior VTA (Yamaguchi et al., 2007; Morales and Root, 2014; Root et al., 2018); thus, it is possible that the null effect of MCH at *Vglut2* cells is ascribed to differences in electrophysiological effects in the anterior and posterior VTA (Guan et al., 2012). It may thus be insightful to track the rostrocaudal distribution of subsequent patch-clamp recordings. In contrast, MCH increased glutamatergic tone at *Th* VTA cells. *Vglut2* VTA cells form local synapses with dopaminergic and nondopaminergic VTA neurons (Dobi et al., 2010) and are pivotal regulators of local VTA circuitry and output. Glutamatergic VTA cells can drive dopamine release and promote conditioned place preference (Wang et al., 2015) or drug-induced conditioned place preference (Tzschentke and Schmidt, 1998; Mead and Stephens, 1999; Slusher et al., 2001) that can be enhanced by food restriction (Stuber et al., 2002) to assess drug reward (Hiroi and White, 1991). Interestingly, *Mchr1* deletion can block the effect of food restriction on amphetamine-induced conditioned place preference (Geuzaine et al., 2014). However, as *Vglut2* cells within the VTA were not MCH-sensitive, it would be important to consider that MCH may indirectly modulate the dopamine output at glutamatergic afferents arising from outside the VTA, such as from the prefrontal cortex (Beier et al., 2015) or lateral hypothalamus (Geisler and Wise, 2008; Watabe-Uchida et al., 2012). Furthermore, since we did not detect postsynaptic MCH effects at the soma of *Vglut2* cells, we predicted that MCHR1 distribution within *Vglut2* cells would accumulate at presynaptic terminals to regulate glutamate release at projection sites (Fig. 9G, asterisk).

Prominent *Vgat* expression in the posterior VTA may partly form the tail of the VTA (tVTA) or rostromedial tegmental nucleus (RMTg; Jhou et al., 2009). The GABAergic cell cluster in the posterior VTA also reflected the highest proportion of *Vgat* VTA cells that expressed *Mchr1*. This supports the hypothesis that the posterior VTA is anatomically and functionally

Figure 7. Rapid detection of direct MCH-mediated hyperpolarization at GABAergic and dopaminergic VTA cells. MCH-sensitive VTA cells identified by a localized puff of MCH applied within 20 μm of the patched cell (***Ai***). Representative sample trace of the membrane potential change following a puff of MCH (red shaded region) lasting <5 s (***Aii***). Δ RMP over time following the first (black circles) and second localized puff (white circles) of 3 μM MCH or of bath ACSF (gray circles) onto a VTA cell (***Aiii***). RMP change over time, or lack of (gray outlined circles), following a localized puff of 3 μM MCH in the presence (red outlined circles) or absence of 500 nM TTX (black circles) at *Vgat*[EGFP] (***B***) and *Th*[EGFP] VTA cells (***C***). Mixed-effect two–way ANOVA: *$p < 0.05$; **$p < 0.01$. Scale bars: ***Ai***, 25 μm; ***Aii***, 3 mV, 10 s.

VTA, we found over 80% of patched EGFP[Th] cells expressed TH, indicating more robust TH expression in EGFP[Th] cells than previously reported.
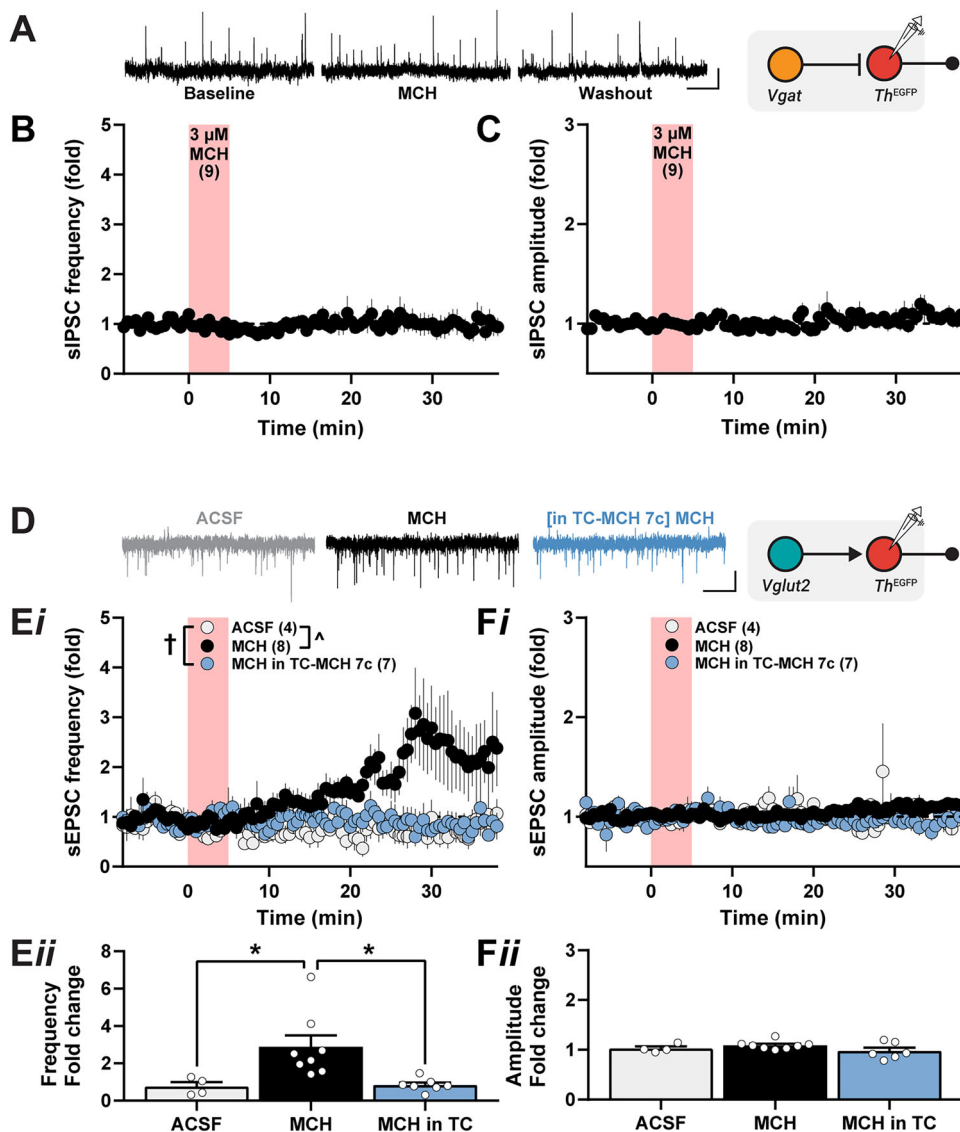
MCHR1 signaling has known inhibitory actions (Chambers et al., 1999; Lembo et al., 1999; Saito et al., 1999; Hawes et al., 2000), including within the mesolimbic system connecting the VTA and ventral striatum. In the accumbens, MCH hyperpolarizes medium spiny neurons (Georgescu et al., 2005) and
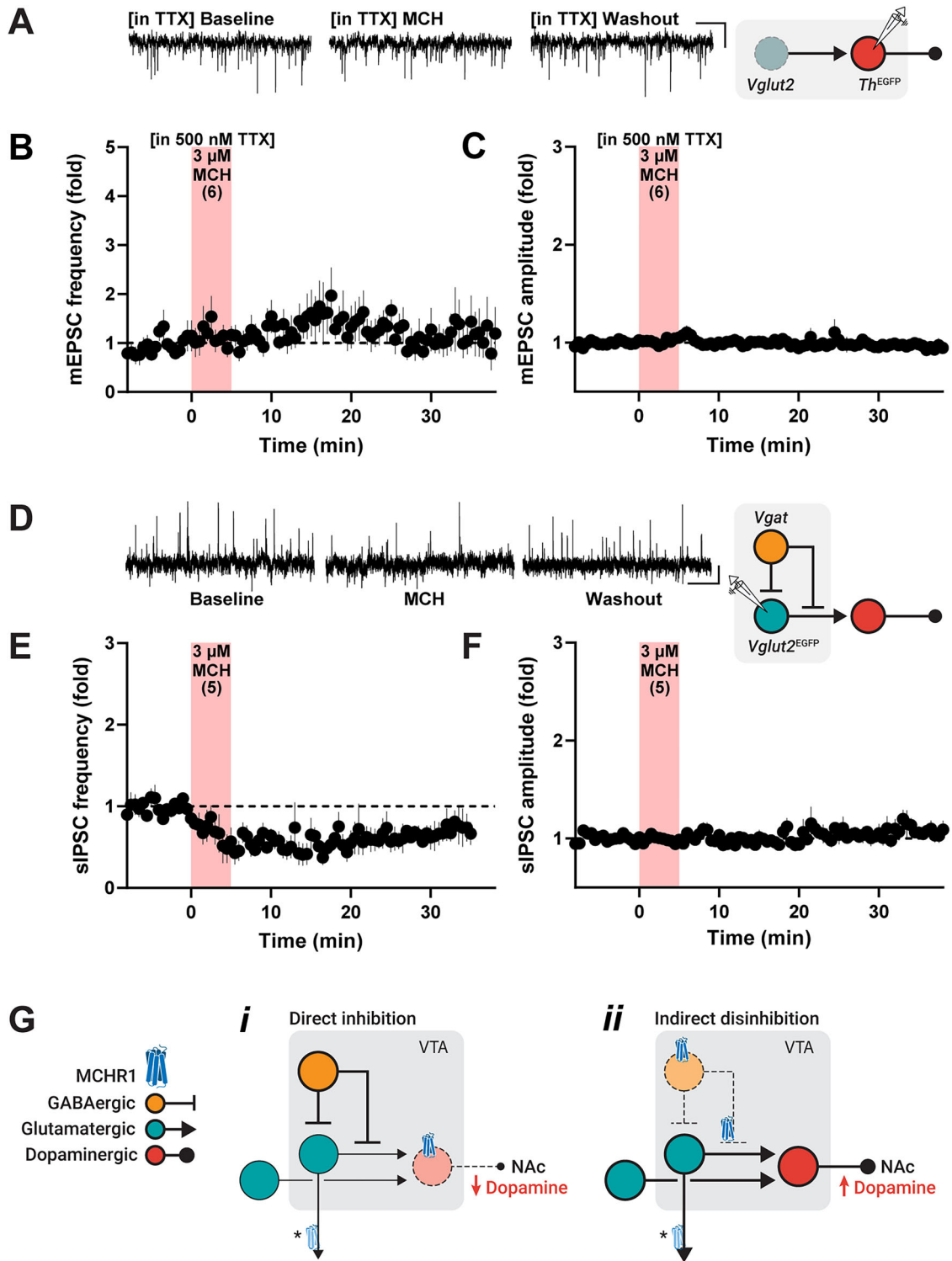
Figure 8. Delayed MCH-mediated increase of excitatory input to Th^{EGFP} VTA cells. Representative sample trace of sIPSC events at the baseline, following 3 µM MCH application, and MCH washout (left) from patch-clamp recordings at Th^{EGFP} cells (right schematic; **A**). Time course of the relative fold change in sIPSC frequency (**B**) and amplitude (**C**) relative to baseline values following bath application of 3 µM MCH. Representative sample trace of sEPSC events in ACSF, 3 µM MCH, and in MCH following pretreatment with 10 µM TC-MCH 7c (left) from patch-clamp recordings at Th^{EGFP} cells (right schematic; **D**). Time course of the relative (**i**) and peak (**ii**) fold change in sEPSC frequency (**E**) and amplitude (**F**) relative to baseline values following bath application of 3 µM MCH (black), bath ACSF only (gray), or MCH after pretreatment with 10 µM TC-MCH 7c (blue) for at least 10 min. One-way ANOVA: *$p < 0.05$ or two-way ANOVA: †$p < 0.05$ with Šidák multiple-comparison post-test: ^$p < 0.05$. Scale bars: 10 pA, 2.5 s (**A,D**).

unique (Lahti et al., 2016; Smith et al., 2019) and suggests that this subregion is a site of MCH action. Sex may interact with *Vgat* expression at *Mchr1* cells in the VTA, as there is a larger portion of *Mchr1* cells expressing *Vgat* in the VTA of female mice. Therefore, MCH may contribute to sex-specific regulation of the VTA output, potentially via *Vgat* cells in females or by yet characterized *Mchr1*-only cells in males. The tVTA/RMTg has been implicated in responsiveness to alcohol as the exposure to alcohol stimulates tVTA/RMTg neurons, and rats will self-administer ethanol to the posterior but not anterior VTA (Guan et al., 2012). Interestingly, *Mchr1* deletion suppresses alcohol-induced conditioned place preference (Karlsson et al., 2016), and MCHR1 blockade decreases self-administration of alcohol (Cippitelli et al., 2010). The posterior VTA supplies dense GABAergic projections to other VTA neurons (Jhou et al., 2009; Barrot et al., 2012; Lecca et al., 2012) and provides strong inhibitory tone to dopaminergic VTA neurons (Barrot et al., 2012;

Guan et al., 2012; Bouarab et al., 2019). While MCH did not regulate GABAergic synaptic transmission at *Th* VTA cells, it inhibited GABAergic transmission at glutamatergic cells. Furthermore, MCH directly inhibited *Vgat* cells; thus, taken together, MCH action at *Vgat* cells in the posterior VTA may weaken inhibition of *Th* VTA cells to indirectly facilitate the dopaminergic output.

Consistent with findings in rats (Hervieu et al., 2000; Saito et al., 2001), the relative expression of *Mchr1* mRNA in the VTA was comparable to that in the hypothalamus and hippocampus. *Mchr1* expression was visible in all major subtypes of VTA cells, including cells that coexpressed two or more chemical messengers. *Vgat/Vglut2* cells were the most common subpopulation coexpressing a combination of TH, *Vgat*, or *Vglut2* and are consistent with previous reports of GABA and glutamate corelease from VTA cells (Root et al., 2014b, 2018). VTA neurons may also be both glutamatergic and dopaminergic (Yamaguchi et al., 2011; Morales and Root,

Figure 9. MCH-mediated disinhibition of local excitatory input to *Th* VTA cells. Representative sample trace of mEPSC events in the presence of 500 nM TTX at the baseline, following 3 µM MCH application, and MCH washout (left) from patch-clamp recordings at *Th*[EGFP] cells (right schematic; **A**). Time course of the relative fold change in mEPSC frequency (**B**) and amplitude (**C**) relative to baseline values following bath application of 3 µM MCH in slices pretreated with 500 nM TTX. Representative sample trace of sIPSC events at the baseline, following 3 µM MCH application, and MCH washout (left) from patch-clamp recordings at *Vglut2*[EGFP] cells (right schematic; **D**). Time course of the relative fold change in sIPSC frequency (**E**) and amplitude (**F**) relative to baseline values following bath application of 3 µM MCH. Model of bidirectional, MCH-mediated regulation of dopamine release from the VTA to nucleus accumbens (NAc) via the mesolimbic pathway (**G**). Schematic showing inferred MCHR1 distribution within the VTA to elicit MCH-mediated direct inhibition of *Th*[EGFP] VTA cells (*i*) and delayed, indirect GABA-mediated disinhibition of glutamatergic input to *Th*[EGFP] VTA cells (*ii*). Putative MCHR1 expression (*) along efferent projections of VTA *Vglut2*[EGFP] cells, which were not MCH-responsive. Scale bars: **A**, 5 pA, 2.5 s; **D**, 10 pA, 2.5 s.

2014; Morales and Margolis, 2017), but unlike the rat VTA, the incidence of colocalization between TH and *Vglut2* was low. In rats, most dopaminergic and glutamatergic VTA cells were at or very close to the midline (Yamaguchi et al., 2011) and includes midline regions encompassing the interfascicular nucleus raphe, rostral linear nucleus raphe, and central linear nucleus raphe as subregions of

the VTA (Yamaguchi et al., 2011; Morales and Root, 2014; Morales and Margolis, 2017). However, our analyses were based on the neuroanatomical boundaries of the VTA as defined by the *ARA* (Dong, 2008) and so did not include the midline outside the VTA where dual TH/*Vglut2* cells may be most abundant. Finally, although VTA cells may corelease dopamine and GABA (Tritsch et al., 2012; Stamatakis et al., 2013), coexpression of TH and *Vgat* did not form a substantial population within the VTA. GABA release does not require vesicular transport via vGAT because the vesicular monoamine transporter 2 can fully support GABA release from dopaminergic cells (Tritsch et al., 2012); thus it is not surprising that TH/*Vgat* coexpression was low.

In conclusion, our findings suggest that MCHR1 expression at multiple VTA cell types can modulate the local VTA microcircuit to provide bidirectional regulation of the dopamine output from the VTA. MCH directly inhibited dopaminergic VTA cells, which may acutely suppress dopamine release. However, MCH also inhibited GABAergic VTA cells, which may disinhibit the glutamatergic input to dopamine cells. This GABA-mediated disinhibition has a delayed time course and may act to restore dopamine levels acutely lowered by the direct MCH-mediated inhibition of dopamine cells. Paradoxically, this may be in contrast to prior findings that *Mchr1* deletion from *Vgat* neurons results in a hyperdopaminergic state (Chee et al., 2019), but this and previous findings may not be mutually exclusive, as MCH can have site-specific effects at different nodes of the mesolimbic dopamine pathway. It would be of interest to test our proposed model (Fig. 9G) in future studies and determine if *Mchr1* deletion from dopaminergic cells would also elicit a hyperdopaminergic state or whether disrupting GABAergic transmission would abolish the facilitation of the glutamatergic input to dopamine cells.

References

Abercrombie M (1946) Estimation of nuclear population from microtome sections. Anat Rec 94:239–247.

Albanese A, Minciacchi D (1983) Organization of the ascending projections from the ventral tegmental area: a multiple fluorescent retrograde tracer study in the rat. J Comp Neurol 216:406–420.

Åstrand A, Bohlooly M, Larsdotter S, Mahlapuu M, Andersén H, Tornell J, Ohlsson C, Snaith M, Morgan DGA (2004) Mice lacking melanin-concentrating hormone receptor 1 demonstrate increased heart rate associated with altered autonomic activity. Am J Physiol 287:749–758.

Bansal R, Engle SE, Kamba TK, Brewer KM, Lewis WR, Berbari NF (2021) Artificial intelligence approaches to assessing primary cilia. J Vis Exp 2021:1–21.

Bariselli S, Glangetas C, Tzanoulinou S, Bellone C (2016) Ventral tegmental area subcircuits process rewarding and aversive experiences. J Neurochem 139:1071–1080.

Barrot M, Sesack SR, Georges F, Pistis M, Hong S, Jhou TC (2012) Braking dopamine systems: a new GABA master structure for mesolimbic and nigrostriatal functions. J Neurosci 32:14094–14101.

Beier KT, Steinberg EE, DeLoach KE, Xie S, Miyamichi0 K, Schwarz L, Gao XJ, Kremer EJ, Malenka RC, Luo L (2015) Circuit architecture of VTA dopamine neurons revealed by systematic input–output mapping. Cell 162:622–634.

Bittencourt JC, Presse F, Arias C, Peto C, Vaughan J, Nahon J-L, Vale W, Sawchenko PE (1992) The melanin-concentrating hormone system of the rat brain: an immuno- and hybridization histochemical characterization. J Comp Neurol 319:218–245.

Bono BS, Koziel Ly NK, Miller PA, Williams-Ikhenoba J, Dumiaty Y, Chee MJ (2022) Spatial distribution of beta-klotho mRNA in the mouse hypothalamus, hippocampal region, subiculum, and amygdala. J Comp Neurol 530:1634–1657.

Bouarab C, Thompson B, Polter AM (2019) VTA GABA neurons at the interface of stress and reward. Front Neural Circuits 13:1–12.

Chambers J, et al. (1999) Melanin-concentrating hormone is the cognate ligand for the orphan G-protein-coupled receptor SLC-1. Nature 400:261–265.

Chee MJ, Hebert AJ, Briançon N, Flaherty SE, Pissios P, Maratos-Flier E (2019) Conditional deletion of melanin-concentrating hormone receptor 1 from GABAergic neurons increases locomotor activity. Mol Metab 29:114–123.

Chee MJ, Myers MG, Price CJ, Colmers WF (2010) Neuropeptide Y suppresses anorexigenic output from the ventromedial nucleus of the hypothalamus. J Neurosci 30:3380–3390.

Chee MJ, Pissios P, Maratos-Flier E (2013) Neurochemical characterization of neurons expressing MCHR1 in mouse hypothalamus. J Comp Neurol 521:2208–2234.

Chen Y, et al. (2002) Targeted disruption of the melanin-concentrating hormone receptor-1 results in hyperphagia and resistance to diet-induced obesity. Endocrinology 143:2469–2477.

Cippitelli A, Karlsson C, Shaw JL, Thorsell A, Gehlert DR, Heilig M (2010) Suppression of alcohol self-administration and reinstatement of alcohol seeking by melanin-concentrating hormone receptor 1 (MCH1-R) antagonism in Wistar rats. Psychopharmacology 211:367–375.

Dal Bo G, St.-Gelais F, Danik M, Williams S, Cotton M, Trudeau LE (2004) Dopamine neurons in culture express VGLUT2 explaining their capacity to release glutamate at synapses in addition to dopamine. J Neurochem 88:1398–1405.

Diniz GB, et al. (2020) Ciliary melanin-concentrating hormone receptor 1 (MCHR1) is widely distributed in the murine CNS in a sex-independent manner. J Neurosci Res 98:2045–2071.

Dobi A, Margolis EB, Wang HL, Harvey BK, Morales M (2010) Glutamatergic and nonglutamatergic neurons of the ventral tegmental area establish local synaptic contacts with dopaminergic and nondopaminergic neurons. J Neurosci 30:218–229.

Domingos AI, et al. (2013) Hypothalamic melanin concentrating hormone neurons communicate the nutrient value of sugar. Elife 2:e01462.

Dong H (2008) *The Allen reference atlas: a digital color brain atlas of the C57BL/6J male mouse.* Hoboken, NJ: John Wiley and Sons.

Faget L, Osakada F, Duan J, Ressler R, Johnson AB, Proudfoot JA, Yoo JH, Callaway EM, Hnasko TS (2016) Afferent inputs to neurotransmitter-defined cell types in the ventral tegmental area. Cell Rep 15:2796–2808.

Gao X-B, van den Pol AN (2001) Melanin concentrating hormone depresses synaptic activity of glutamate and GABA neurons from rat lateral hypothalamus. J Physiol 533:237–252.

Geisler S, Wise RA (2008) Functional implications of glutamatergic projections to the ventral tegmental area. Rev Neurosci 19:227–244.

Georgescu D, et al. (2005) The hypothalamic neuropeptide melanin-concentrating hormone acts in the nucleus accumbens to modulate feeding behavior and forced-swim performance. J Neurosci 25:2933–2940.

Geuzaine A, Tyhon A, Grisar T, Brabant C, Lakaye B, Tirelli E (2014) Amphetamine reward in food restricted mice lacking the melanin-concentrating hormone receptor-1. Behav Brain Res 262:14–20.

Guan Y, Xiao C, Krnjević K, Xie G, Zuo W, Ye J-H (2012) GABAergic actions mediate opposite ethanol effects on dopaminergic neurons in the anterior and posterior ventral tegmental area. J Pharmacol Exp Ther 341:33–42.

Hawes BE, Erin KIL, Green B, O'Neill KIM, Fried S, Graziano MP (2000) The melanin-concentrating hormone receptor couples to multiple G proteins to activate diverse intracellular signaling pathways. Endocrinology 141:4524–4532.

Hervieu GJ, Cluderay JE, Harrison D, Meakin J, Maycox P, Nasir S, Leslie RA (2000) The distribution of the mRNA and protein products of the melanin-concentrating hormone (MCH) receptor gene, slc-1, in the central nervous system of the rat. Eur J Neurosci 12:1194–1216.

Hiroi N, White NM (1991) The amphetamine conditioned place preference: differential involvement of dopamine receptor subtypes and two dopaminergic terminal areas. Brain Res 552:141–152.

Jhou T, Fields H, Baxter M, Saper C (2009) The rostromedial tegmental nucleus (RMTg), a major GABAergic afferent to midbrain dopamine neurons, selectively encodes aversive stimuli and promotes behavioral inhibition. Neuron 61:786–800.

Karlsson C, Rehman F, Damdazic R, Atkins AL, Schank JR, Gehlert DR, Steensland P, Thorsell A, Heilig M (2016) The melanin-concentrating hormone-1 receptor modulates alcohol-induced reward and DARPP-32 phosphorylation. Psychopharmacology 233:2355–2363.

Kokkotou E, Jeon JY, Wang X, Marino FE, Carlson M, Trombly DJ, Maratos-Flier E (2005) Mice with MCH ablation resist diet-induced obesity through strain-specific mechanisms. Am J Physiol Regul Integr Comp Physiol 289:117–124.

Krashes MJ, et al. (2014) An excitatory paraventricular nucleus to AgRP neuron circuit that drives hunger. Nature 507:238–242.

Lahti L, Haugas M, Tikker L, Airavaara M, Voutilainen MH, Anttila J, Kumar S, Inkinen C, Salminen M, Partanen J (2016) Differentiation and molecular heterogeneity of inhibitory and excitatory neurons associated with midbrain dopaminergic nuclei. Development 143:516–529.

Lammel S, Steinberg EE, Földy C, Wall NR, Beier K, Luo L, Malenka RC (2015) Diversity of transgenic mouse models for selective targeting of midbrain dopamine neurons. Neuron 85:429–438.

Lecca S, Melis M, Luchicchi A, Muntoni AL, Pistis M (2012) Inhibitory inputs from rostromedial tegmental neurons regulate spontaneous activity of midbrain dopamine cells and their responses to drugs of abuse. Neuropsychopharmacology 37:1164–1176.

Lembo PMC, et al. (1999) The receptor for the orexigenic peptide melanin-concentrating hormone is a G-protein-coupled receptor. Nat Cell Biol 1:267–271.

Lindeberg J, Usoskin D, Bengtsson H, Gustafsson A, Kylberg A, Söderström S, Ebendal T (2004) Transgenic expression of Cre recombinase from the tyrosine hydroxylase locus. Genesis 40:67–73.

Lord MN, Subramanian K, Kanoski SE, Noble EE, Angeles L, Section EB, California S, Angeles L (2022) Melanin-concentrating hormone and food intake control: sites of action, peptide interactions, and appetition. Peptides 137:1–23.

Ludwig DS, Tritos NA, Mastaitis JW, Kulkarni R, Kokkotou E, Elmquist J, Lowell B, Flier JS, Maratos-Flier E (2001) Melanin-concentrating hormone overexpression in transgenic mice leads to obesity and insulin resistance. J Clin Invest 107:379–386.

Marsh DJ, et al. (2002) Melanin-concentrating hormone 1 receptor-deficient mice are lean, hyperactive, and hyperphagic and have altered metabolism. Proc Natl Acad Sci U S A 99:3240–3245.

Mead AN, Stephens DN (1999) CNQX but not NBQX prevents expression of amphetamine-induced place preference conditioning: a role for the glycine site of the NMDA receptor, but not AMPA receptors. J Pharmacol Exp Ther 290:9–15.

Mickelsen LE, Bolisetty M, Chimileski BR, Fujita A, Beltrami EJ, Costanzo JT, Naparstek JR, Robson P, Jackson AC (2019) Single-cell transcriptomic analysis of the lateral hypothalamic area reveals molecularly distinct populations of inhibitory and excitatory neurons. Nat Neurosci 22:642–656.

Morales M, Margolis EB (2017) Ventral tegmental area: cellular heterogeneity, connectivity and behaviour. Nat Rev Neurosci 18:73–85.

Morales M, Root DH (2014) Glutamate neurons within the midbrain dopamine regions. Neuroscience 282:60–68.

Mul JD, et al. (2011) Chronic loss of melanin-concentrating hormone affects motivational aspects of feeding in the rat. PLoS One 6:e19600.

Negishi K, Payant MA, Schumacker KS, Wittmann G, Butler RM, Lechan RM, Steinbusch HWM, Khan AM, Chee MJ (2020) Distributions of hypothalamic neuron populations coexpressing tyrosine hydroxylase and the vesicular GABA transporter in the mouse. J Comp Neurol 528:1833–1855.

Nieh EH, Vander Weele CM, Matthews GA, Presbrey KN, Wichmann R, Leppla CA, Izadmehr EM, Tye KM (2016) Inhibitory input from the lateral hypothalamus to the ventral tegmental area disinhibits dopamine neurons and promotes behavioral activation. Neuron 90:1286–1298.

Pissios P, Frank L, Kennedy AR, Porter DR, Marino FE, Liu FF, Pothos EN, Maratos-Flier E (2008) Dysregulation of the mesolimbic dopamine system and reward in MCH-/- mice. Biol Psychiatry 64:184–191.

Pissios P, Trombly DJ, Tzameli I, Maratos-Flier E (2003) Melanin-concentrating hormone receptor 1 activates extracellular signal-regulated kinase and synergizes with Gs-coupled pathways. Endocrinology 144:3514–3523.

Qu D, Ludwig DS, Gammeltoft S, Piper M, Pelleymountert MA, Cullent MJ, Mathes WF, Przypek J, Kanarek R, Ii EM (1996) A role for melanin-concentrating hormone in the central regulation of feeding behaviour. Nature 380:243–247.

Advanced Cell Diagnostics (2020) RNAscope ® multiplex fluorescent v2 assay combined with immunofluorescence - integrated co-detection workflow (ICW) combinations. Advanced Cell Diagnostics Inc., 1–5.

Root DH, Mejias-Aponte CA, Qi J, Morales M (2014a) Role of glutamatergic projections from ventral tegmental area to lateral habenula in aversive conditioning. J Neurosci 34:13906–13910.

Root DH, Mejias-Aponte CA, Zhang S, Wang HL, Hoffman AF, Lupica CR, Morales M (2014b) Single rodent mesohabenular axons release glutamate and GABA. Nat Neurosci 17:1543–1551.

Root DH, Zhang S, Barker DJ, Miranda-Barrientos J, Liu B, Wang HL, Morales M (2018) Selective brain distribution and distinctive synaptic architecture of dual glutamatergic-GABAergic neurons. Cell Rep 23:3465–3479.

Saito Y, Cheng M, Leslie FM, Civelli O (2001) Expression of the melanin-concentrating hormone (MCH) receptor mRNA in the rat brain. J Comp Neurol 435:26–40.

Saito Y, Nothacker H, Wang Z, Lin SHS, Leslie F, Civelli O (1999) Molecular characterization of the melanin-concentrating- hormone receptor. Nature 400:265–269.

Schneeberger M, Tan K, Nectow AR, Parolari L, Caglar C, Azevedo E, Li Z, Domingos A, Friedman JM (2018) Functional analysis reveals differential effects of glutamate and MCH neuropeptide in MCH neurons. Mol Metab 13:83–89.

Sears RM, Liu RJ, Narayanan NS, Sharf R, Yeckel MF, Laubach M, Aghajanian GK, DiLeone RJ (2010) Regulation of nucleus accumbens activity by the hypothalamic neuropeptide melanin-concentrating hormone. J Neurosci 30:8263–8273.

Shimada M, Tritos NA, Lowell BB, Flier JS, Maratos-Flier E (1998) Mice lacking melanin- concentrating hormone are hypophagic and lean. Nature 396:3–7.

Slusher BS, Thomas A, Paul M, Schad CA, Ashby CR (2001) Expression and acquisition of the conditioned place preference response to cocaine in rats is blocked by selective inhibitors of the enzyme N-acetylated-α-linked-acidic dipeptidase (NAALADase). Synapse 41:22–28.

Smith RJ, Vento PJ, Chao YS, Good CH, Thomas C, Ground AP (2019) Gene expression and neurochemical characterization of the rostromedial tegmental nucleus (RMTg) in rats and mice. Brain Struct Funct 224:219–238.

Stamatakis AM, Jennings JH, Ung RL, Blair GA, Weinberg J, Neve RL, Boyce F, Mattis J, Deisseroth K, Stuber GD (2013) A unique population of ventral tegmental area neurons inhibits the lateral habenula to promote reward. Neuron 80:1–23.

Stuber GD, Evans SB, Higgins MS, Pu Y, Figlewicz DP (2002) Food restriction modulates amphetamine-conditioned place preference and nucleus accumbens dopamine release in the rat. Synapse 46:83–90.

Stuber GD, Hnasko TS, Britt JP, Edwards RH, Bonci A (2010) Dopaminergic terminals in the nucleus accumbens but not the dorsal striatum corelease glutamate. J Neurosci 30:8229–8233.

Sulzer D, Joyce MP, Lin L, Geldwert D, Haber SN, Hattori T, Rayport S (1998) Dopamine neurons make glutamatergic synapses in vitro. J Neurosci 18:4588–4602.

Tecuapetla F, et al. (2010) Glutamatergic signaling by mesolimbic dopamine neurons in the nucleus accumbens. J Neurosci 30:7105–7110.

Ting JT, Lee BR, Chong P, Soler-Llavina G, Cobbs C, Koch C, Zeng H, Lein E (2018) Preparation of acute brain slices using an optimized N-methyl-D-glucamine protective recovery method. J Vis Exp 132:1–13.

Tritsch NX, Ding JB, Sabatini BL (2012) Dopaminergic neurons inhibit striatal output via non-canonical release of GABA. Nature 490:262–266.

Tzschentke TM, Schmidt WJ (1998) Blockade of morphine- and amphetamine-induced conditioned place preference in the rat by riluzole. Neurosci Lett 242:114–116.

Vong L, Ye C, Yang Z, Choi B, Chua S Jr, Lowell BB (2011) Leptin action on GABAergic neurons prevents obesity and reduces inhibitory tone to POMC neurons. Neuron 71:142–154.

Wang HL, Qi J, Zhang S, Wang H, Morales M (2015) Rewarding effects of optical stimulation of ventral tegmental area glutamatergic neurons. J Neurosci 35:15948–15954.

Watabe-Uchida M, Zhu L, Ogawa SK, Vamanrao A, Uchida N (2012) Whole-brain mapping of direct inputs to midbrain dopamine neurons. Neuron 74:858–873.

Yamaguchi T, Sheen W, Morales M (2007) Glutamatergic neurons are present in the rat ventral tegmental area. Eur J Neurosci 25:106–118.

Yamaguchi T, Wang HL, Li X, Ng TH, Morales M (2011) Mesocorticolimbic glutamatergic pathway. J Neurosci 31:8476–8490.